

Supporting Information for:

Alkaline-Earth and Aminonicotinate Based Coordination Polymers with Combined Fluorescence/Long-Lasting Phosphorescence and Metal Ions Sensing Response

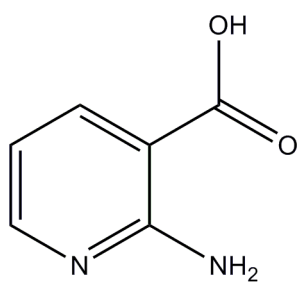
Oier Pajuelo-Corral,^a Antonio Rodríguez-Diéguez,^b Garikoitz Beobide,^c Sonia Pérez-Yáñez,^c Jose A. García,^d Eider San Sebastián,^a Jose M. Seco,^{a*} and Javier Cepeda^{a*}

^a Departamento de Química Aplicada, Facultad de Química, Universidad del País Vasco (UPV/EHU), 20018 Donostia, Spain. ^b Departamento de Química Inorgánica, Facultad de Ciencia y Tecnología, Universidad del País Vasco (UPV/EHU), 48940 Leioa, Spain. ^c Departamento de Química Inorgánica, Facultad de Ciencias, Universidad de Granada, 18071 Granada, Spain. ^d Departamento de Física Aplicada II, Facultad de Ciencia y Tecnología, Universidad del País Vasco (UPV/EHU), 48940 Leioa, Spain.

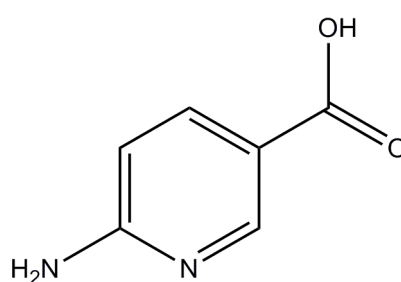
Contents:

- S1. Chemical structures of H2ani and H6ani ligands.
- S2. Chemical characterization of compounds.
- S3. FT-IR spectroscopy.
- S4. Powder X-ray diffraction analysis.
- S5. Structural details of compounds **1**, **3**, and **4**.
- S6. Diffuse reflectance results for compounds **1**, **2**, **4**, **5** and **6**.
- S7. Photoluminescence measurements.
- S8. Lifetime measurements.
- S9. TD-DFT computational details.
- S10. Calculation of the lowest-lying triplet state \rightarrow ground state ($T_1 \rightarrow S_0$) energy.
- S11. PL sensing of compound **4**.

S1. Chemical structures of H2ani and H6ani ligands.



(a)



(b)

Figure S1. Diagrams of the chemical structure of **(a)** H2ani and **(b)** H6ani ligands.

S2. Chemical characterization of compounds.

Table S1. Elemental analysis and TG/DTA curves of compound 1.

[Sr(μ -2ani)(μ ₃ -2ani)(μ -DMF)] _n		
C ₁₅ H ₁₇ N ₅ O ₅ Sr → M.W. = 434.95 g/mol		
Ti-Tf	$\Sigma\Delta m(\%)$	$\Sigma\Delta m(\%)_{\text{theor}}$
160–215	17.0	16.8 (–DMF)
345–530	66.2	65.9 (SrCO ₃)

Elemental analysis

Anal. Calc.: C, 41.42; H, 3.94; N, 16.10; Sr, 20.14.

Found: C, 41.84; H, 3.74; N, 16.28; Sr, 19.86%.

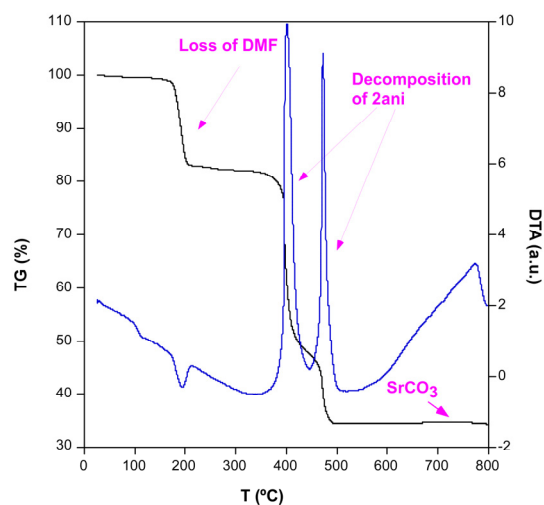


Table S2. Elemental analysis and TG/DTA curves of compound 2.

[Ba(μ -2ani)(μ ₃ -2ani)(μ -DMF)] _n		
C ₁₅ H ₁₇ BaN ₅ O ₅ → M.W. = 484.65 g/mol		
Ti-Tf	$\Sigma\Delta m(\%)$	$\Sigma\Delta m(\%)_{\text{theor}}$
165–225	15.5	15.1 (–DMF)
325–615	59.6	59.3 (BaCO ₃)

Elemental analysis

Anal. Calc.: C, 37.17; H, 3.54; Ba, 28.34; N, 14.45.

Found: C, 37.10; H, 3.50; Ba, 28.16; N, 14.19%.

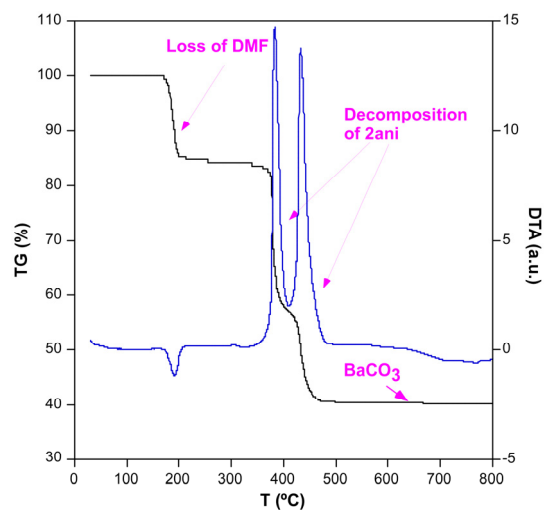
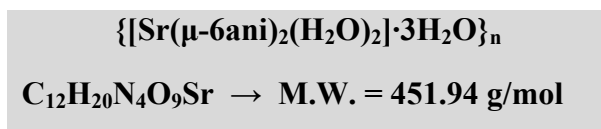


Table S3. Elemental analysis and TG/DTA curves of compound 4.



Ti-Tf	$\Sigma\Delta m(\%)$	$\Sigma\Delta m(\%)_{\text{theor}}$
30–105	12.3	11.9 (–3 H ₂ O)
120–210	20.2	19.8 (–2 H ₂ O)
305–525	68.6	67.4 (SrCO ₃)

Elemental analysis

Anal. Calc.: C, 31.89; H, 4.46; N, 12.40; Sr, 19.39.
 Found: C, 31.73; H, 4.24; N, 12.28; Sr, 19.56%.

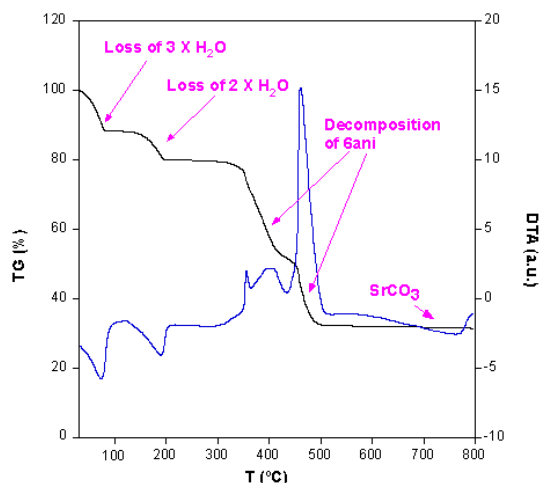
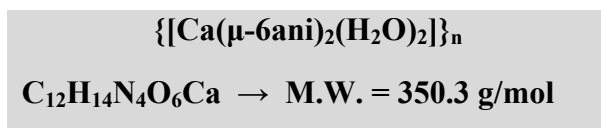


Table S4. Elemental analysis and TG/DTA curves of compound 5.



Ti-Tf	$\Sigma\Delta m(\%)$	$\Sigma\Delta m(\%)_{\text{theor}}$
150-235	10.2	10.3 (–2 H ₂ O)
325-660	83.8	84.0 (CaO)

Elemental analysis

Anal. Calc.: C, 41.14; H, 4.03; Ca, 11.44; N, 16.00.
 Found: C, 41.22; H, 4.11; Ca, 11.68; N, 15.89%.

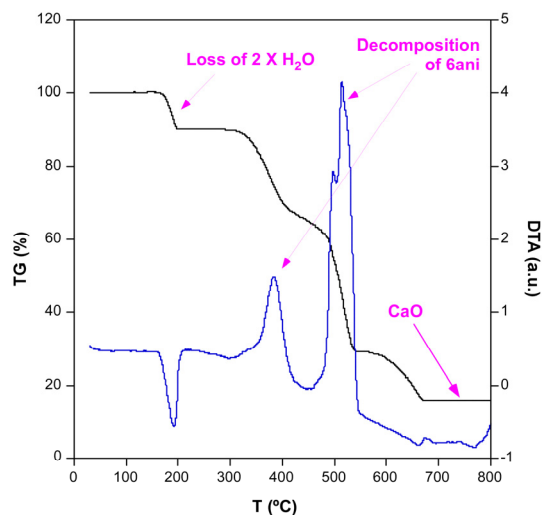
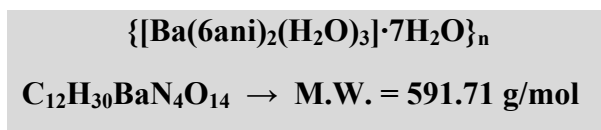


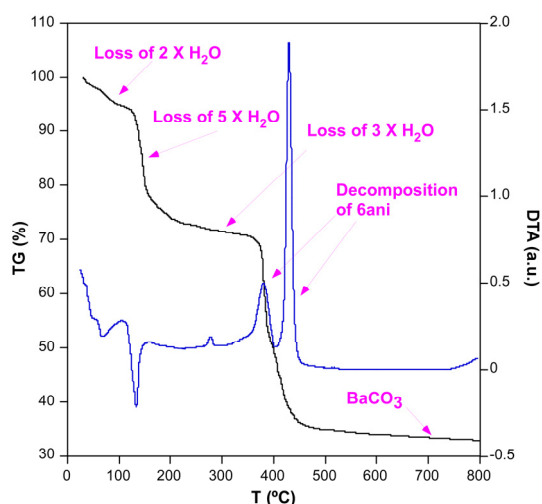
Table S5. Elemental analysis and TG/DTA curves of compound 6.



Ti-Tf	$\Sigma\Delta m(\%)$	$\Sigma\Delta m(\%)_{\text{theor}}$
30–120	5.4	6.1 (–2 H ₂ O)
120–160	21.4	21.3 (–5 H ₂ O)
160–290	29.8	30.4 (–3 H ₂ O)
320–760	66.7	66.6 (BaCO ₃)

Elemental analysis

Anal. Calc.: C: 24.36; H: 5.11; Ba, 23.21; N: 9.47.
 Found: C, 24.63; H, 4.98; Ba, 23.38; N, 9.09%.



S3. FTIR spectroscopy.

As it can be seen in Figure S2, FTIR spectra of compounds **1** and **2** are almost identical and slightly different compared with the H2ani ligand spectrum. At high frequencies, **1** and **2** show some intense band in the 3400-3200 cm^{-1} region corresponding to the exocyclic amino group. The weak bands that appear between 3000-2800 cm^{-1} are due to the presence of the DMF molecule. Several bands appear in the 1650-1600 cm^{-1} region as a consequence of the oxophilic character of the alkaline-earth metals that forms several bonds between the carboxylate oxygen atoms and the metal, which are attributed to the asymmetric vibrations of the carboxylate group. Many intense bands corresponding to the C-C and C-N bonds of the aromatic ring occur in the 1600-1400 cm^{-1} range, while the symmetric stretching vibrations of the carboxylate groups occur in the range of 1400-1200 cm^{-1} . At lower frequencies, the remaining bands can be assigned to the distortions occurring in the aromatic ring and the carboxylate group of the 2ani ligands. The vibrations bands of the M-O and M-N bonds appear around 600-500 cm^{-1} .

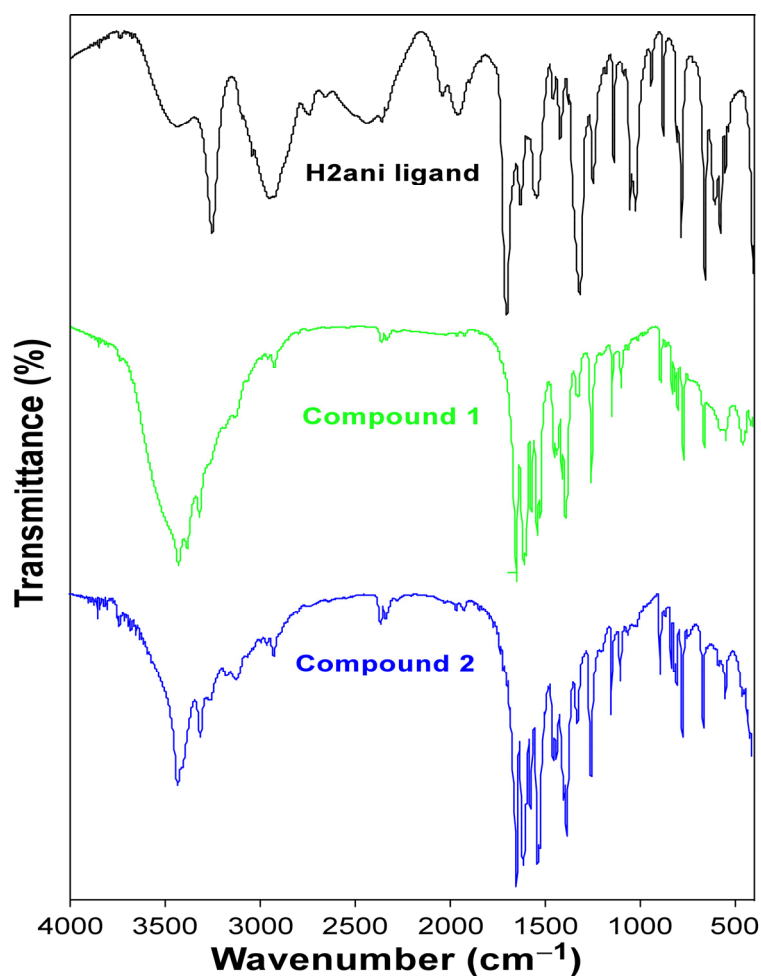


Figure S2. IR spectra of 2ani based compounds **1** and **2**.

FTIR spectra of compounds **4** and **5** look similar, showing bands that appear in the 3400-3200 cm^{-1} range can be assigned to the exocyclic amino group. As occurs in compounds **1** and **2**, several bands appear in the 1650-1600 cm^{-1} region as a consequence of the oxophilic character of these metals that correspond to the asymmetric stretching vibrations of the carboxylate group. Between 1500 and 1200 cm^{-1} , the bands can be assigned to the C-C and C-N vibrations of the pyridine ring and to the symmetric vibrations of the carboxylate. In the 600-500 cm^{-1} region appear some bands due to the M-O and M-N vibrations. On another level, the spectrum of **6** differs slightly from those of **4** and **5** particularly for the region involving the asymmetric stretchings of carboxylate group. In this region, it is worth noticing the occurrence of additional bands, mainly a band peaking at 1675 cm^{-1} , which seems to indicate the presence of various coordination modes of 6ani ligands coexisting in the compound.

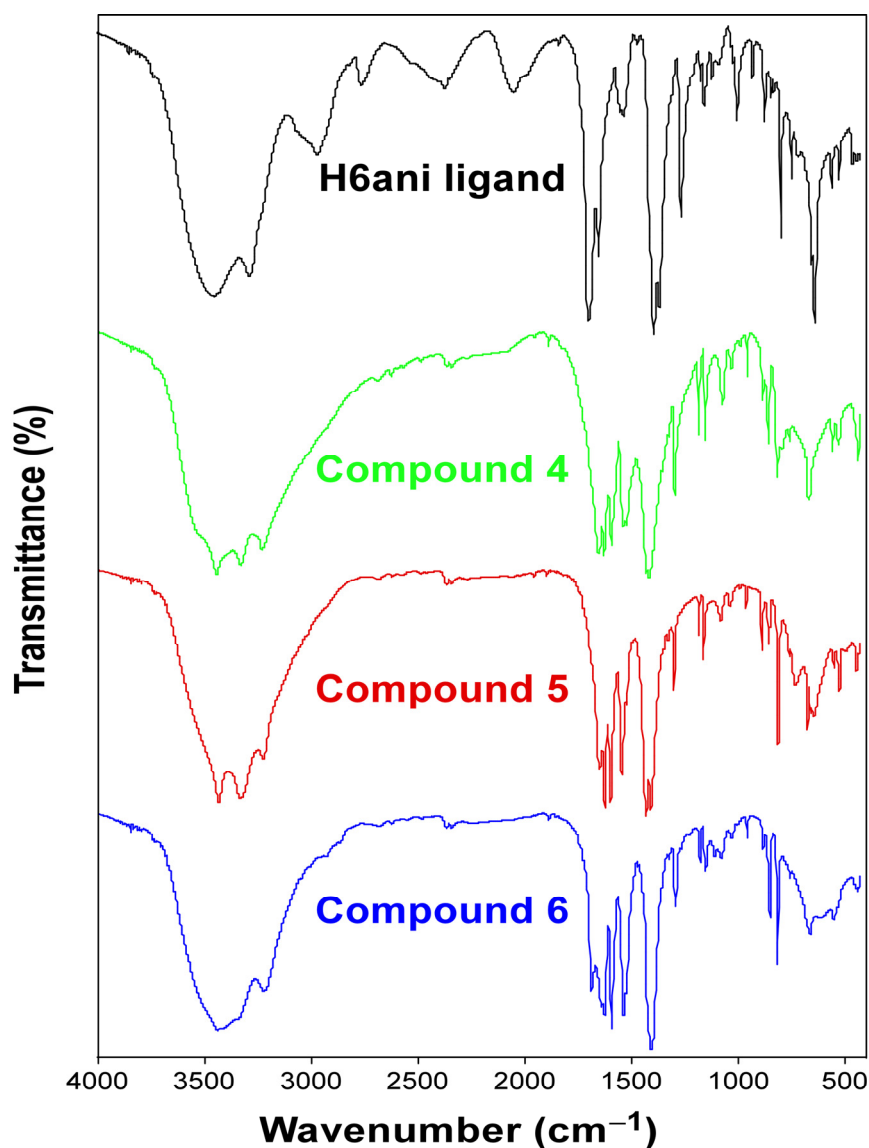


Figure S3. IR spectra of 6ani based compounds **4**, **5** and **6**.

Calculated FTIR spectra computed by DFT

With the aim of better understanding the origin of the bands observed in the FTIR spectrum of compound **6**, we have carried out a systematic analysis of the most representative (see Scheme 1 in the manuscript) coordination modes already shown by 6ani ligand in the bibliography (Figure S4). Calcium ion has been employed instead of heavy barium ions. As observed in the modes assigned below, the coordination of N_{pyridine} atom brings a significant shift of the main vibration band related to the aromatic ring deformation and asymmetric stretching of carboxylate group to longer wavenumbers (up to 1680 cm^{-1}) in the calculation of mode c. Therefore, the good agreement between the calculated and experimental wavenumber (1680 cm^{-1} vs 1675 cm^{-1}) suggests the occurrence of AE- N_{pyridine} coordination in the structure of compound **6**.

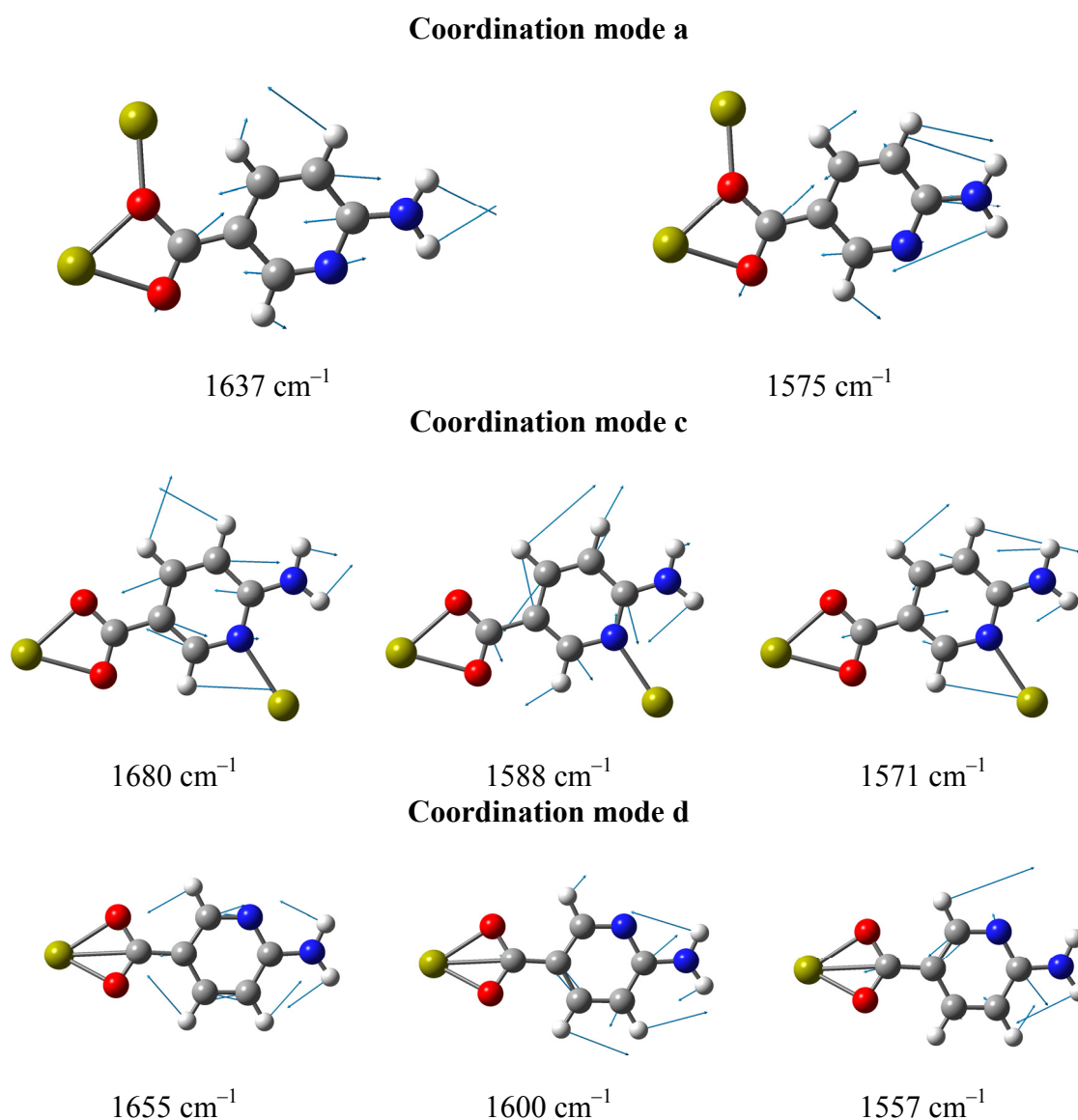


Figure S4. IR modes for selected coordination modes of 6ani with calcium(II) ions.

S4. Powder X-ray diffraction analysis.

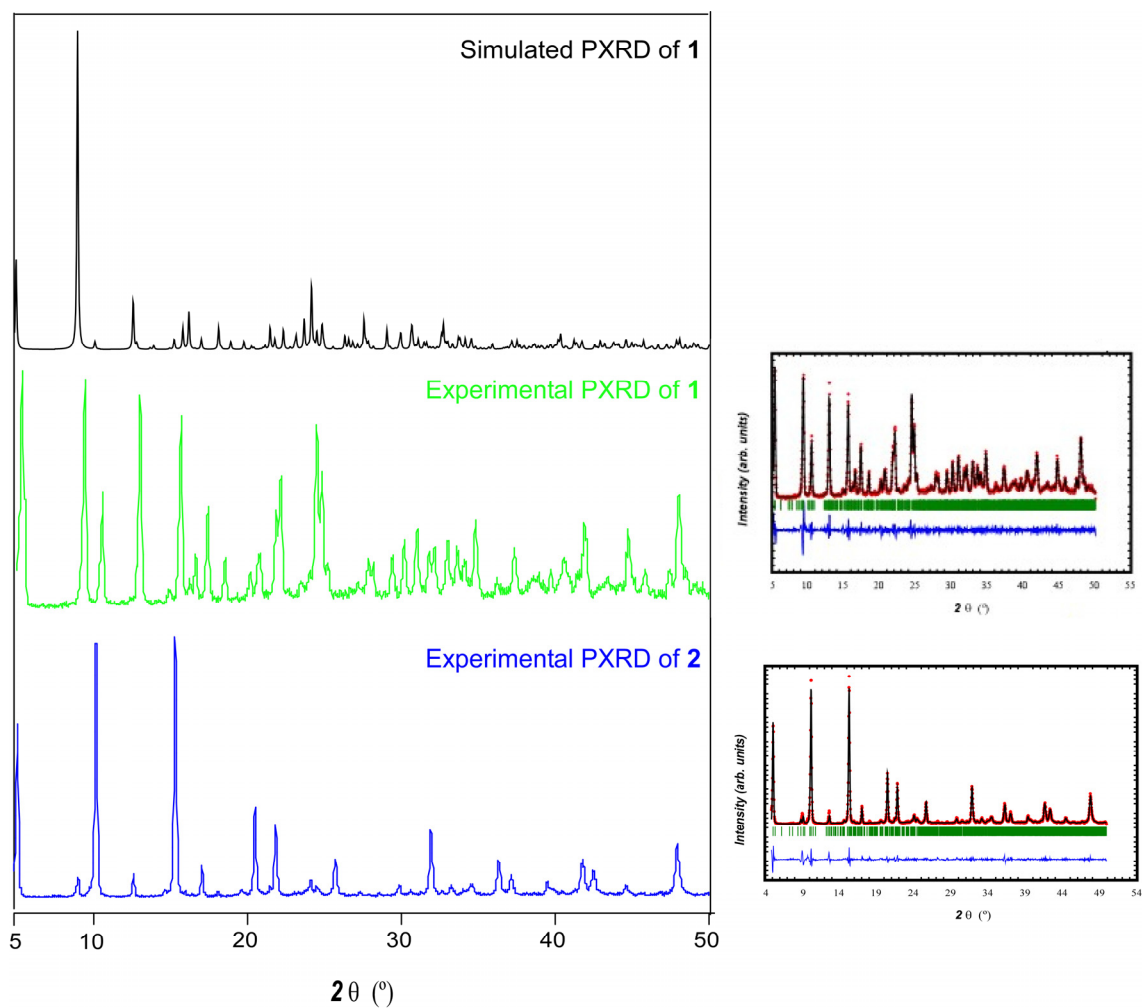


Figure S5. Comparison between the experimental PXRD data for compounds **1** and **2** with that simulated from crystal structure of **1**. Pattern-matching analyses are also shown.

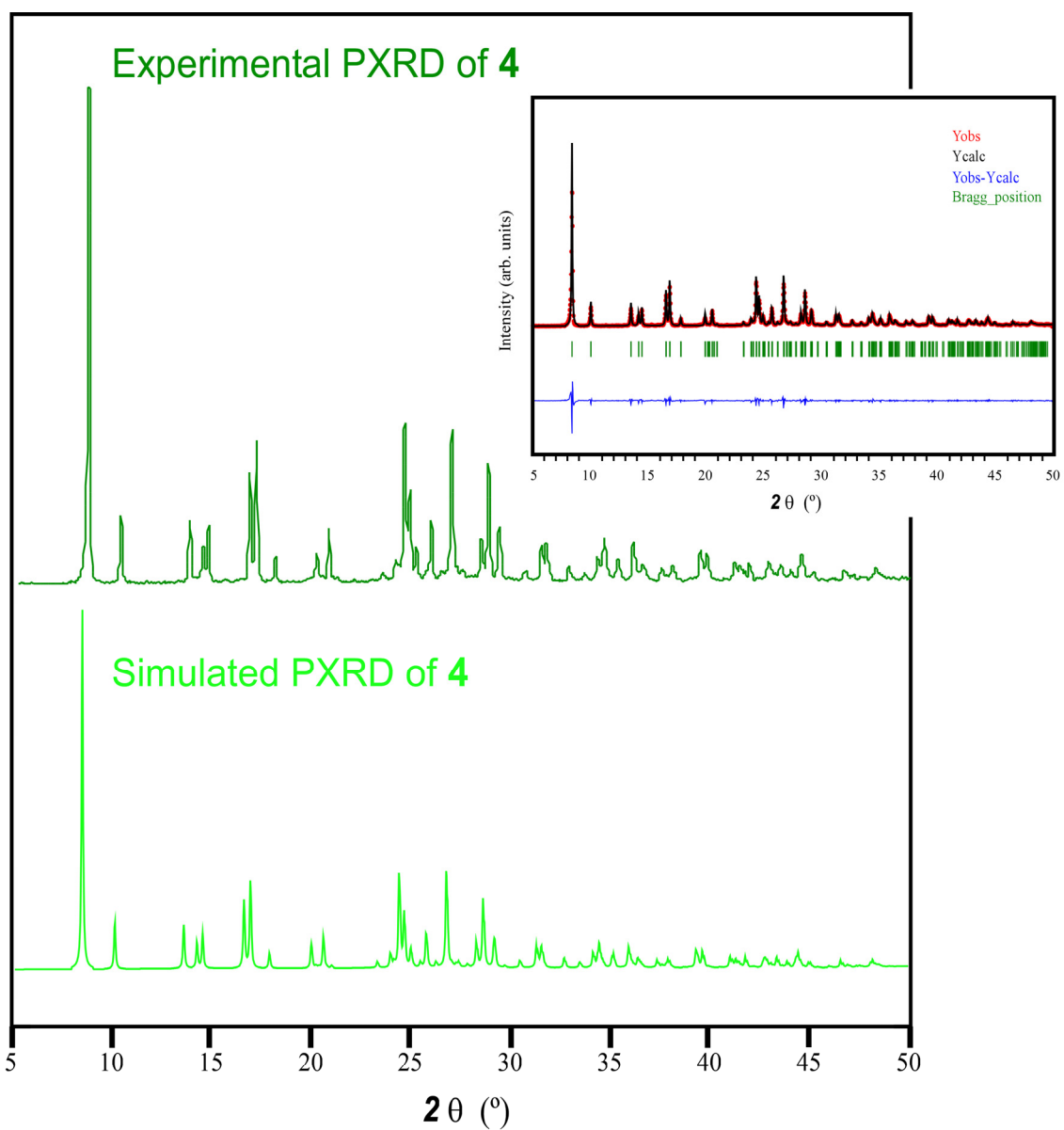


Figure S6. Comparison between the experimental PXRD data for compound **4** with that simulated from crystal structure of **4**. Inset represents the pattern-matching analysis.

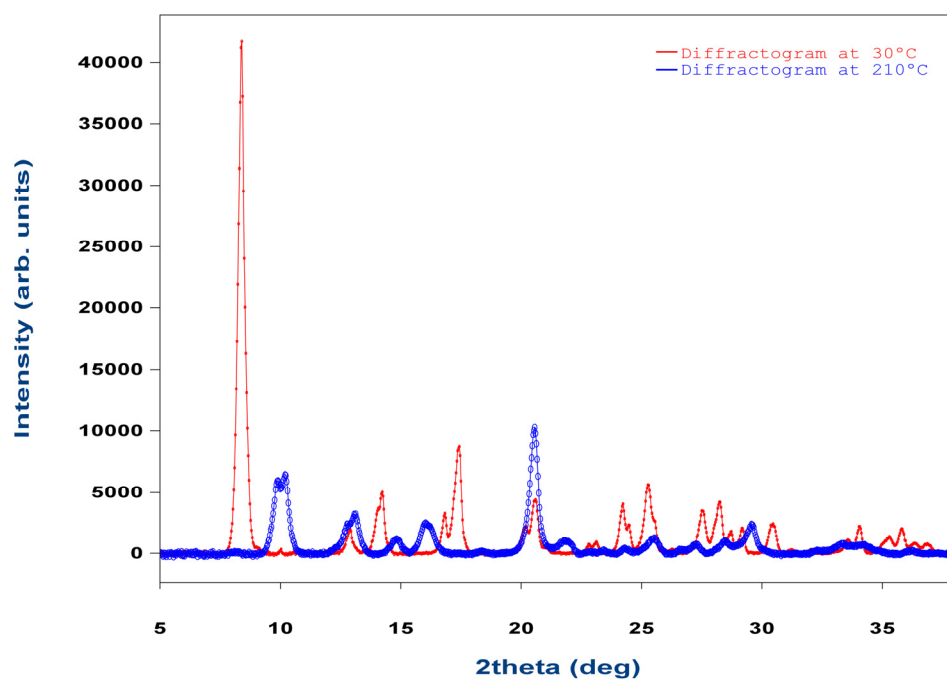


Figure S7. Comparison of the PXRD data for compound **4** at variable temperature. PXRD of compound **4** (red) and PXRD of compound **4-d** (blue).

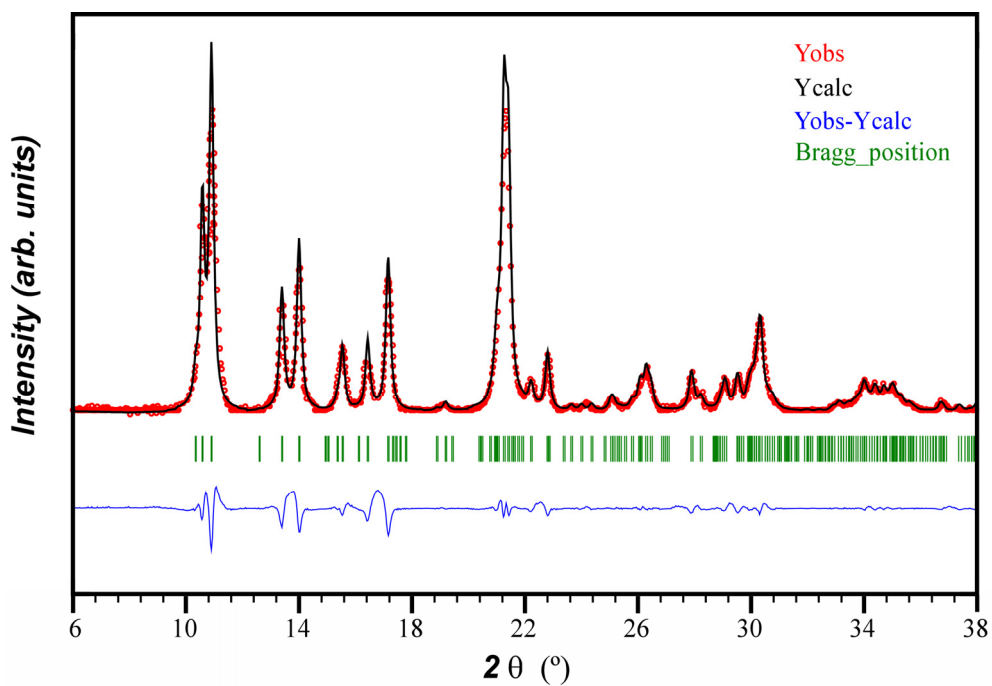


Figure S8. Pattern-matching refinement of **4-d** collected at 210 °C.

When compound **4** is immersed in DMF to undertake the evaluation of its photoluminescence response to that solvent, it exchanges DMF by part of the water molecules in its crystal structure. Nonetheless, the crystal structure is not disrupted since it retains the PXRD pattern but for some slight shifts.

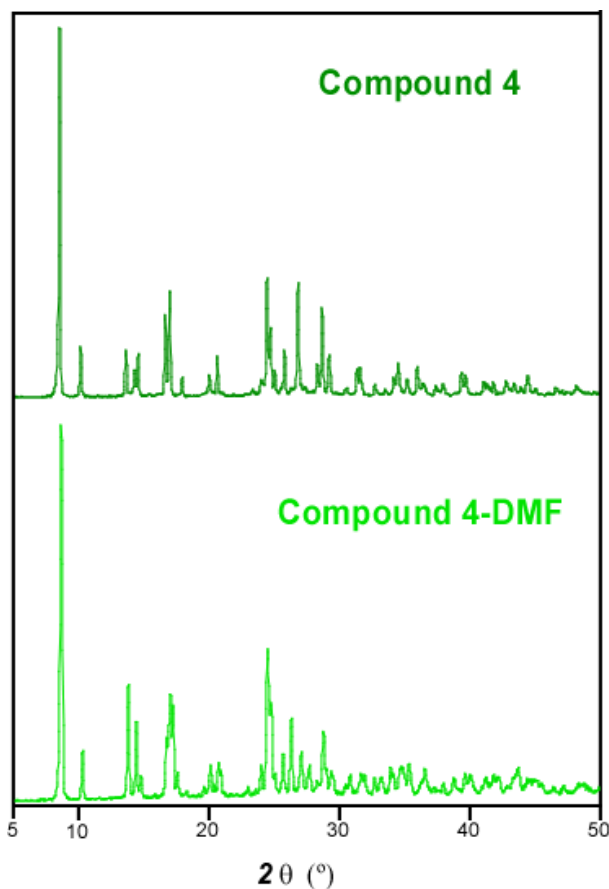


Figure S9. Comparison between PXRD of compound **4** and **4-DMF**.

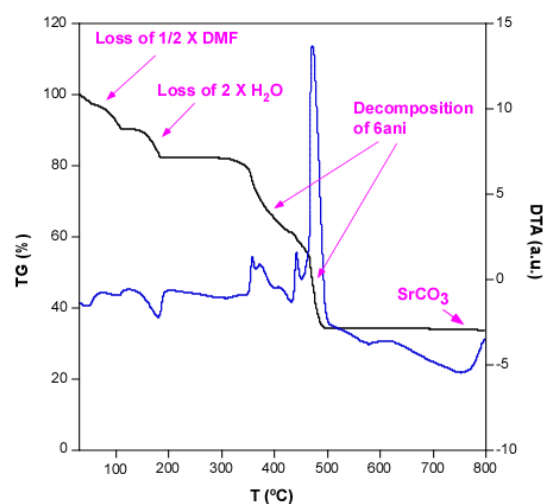
As inferred from TG curve, the first loss is attributed to the replaced DMF molecules, which is released at low temperature since they are weakly bound to the structure as a consequence of the solvent exchange taking place.

Table S6. Elemental analysis and TG/DTA curves of compound **4-DMF**.

$\{[\text{Sr}(\mu\text{-6ani})_2(\text{H}_2\text{O})_2] \cdot 0.5 \text{ DMF}\}_n$ $\text{C}_{13.5}\text{H}_{17.5}\text{N}_{4.5}\text{O}_{6.5}\text{Sr} \rightarrow \text{M.W.} = 434.43 \text{ g/mol}$		
Ti-Tf	$\Sigma\Delta m(\%)$	$\Sigma\Delta m(\%)_{\text{teor}}$
40-130	10.1	8.3 (-1/2 DMF)
140-200	17.8	16.7 (-2H ₂ O)
260-410	65.5	65.9 (SrCO ₃)

Elemental analysis

Anal. Calc.: C, 37.32; H, 4.06; N, 14.51; Sr, 20.17.
 Found: C, 36.98; H, 4.12; N, 14.70; Sr, 20.36%.



On the other hand, the presence of DMF in this sample is observed by the occurrence of weak bands peaking at 2850 and 2925 cm^{-1} which are attributed to the C–H stretching vibrations of the methyl groups.

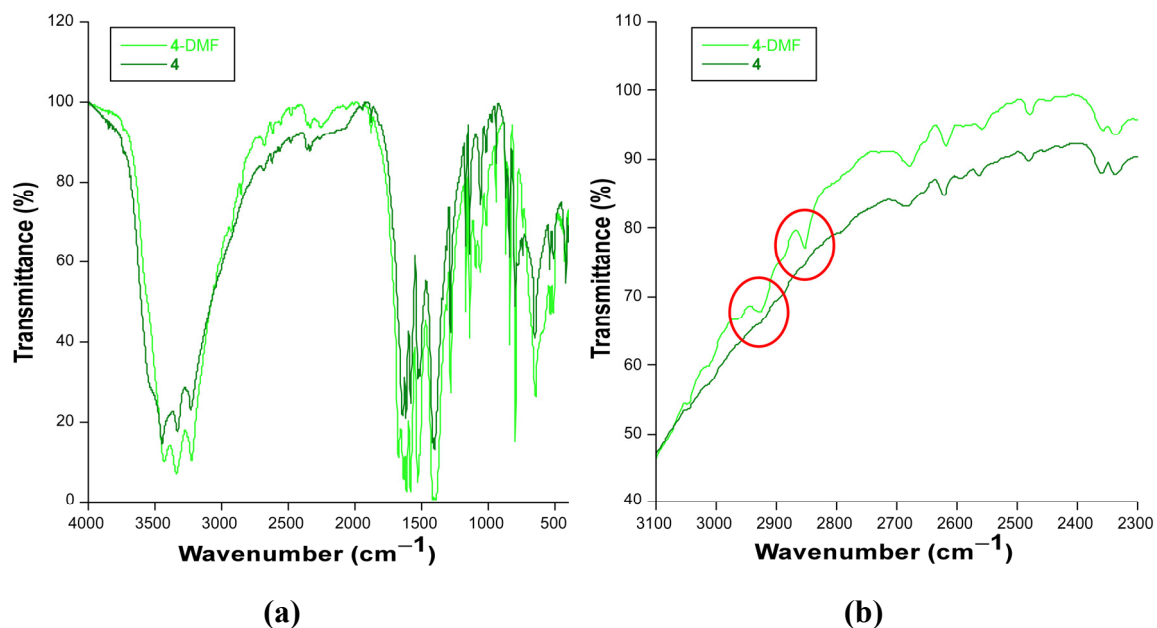


Figure S10. Comparative view of FTIR spectra of compounds **4** and **4-DMF**: (a) in the whole measured wavenumber range and (b) caption with most significant bands.

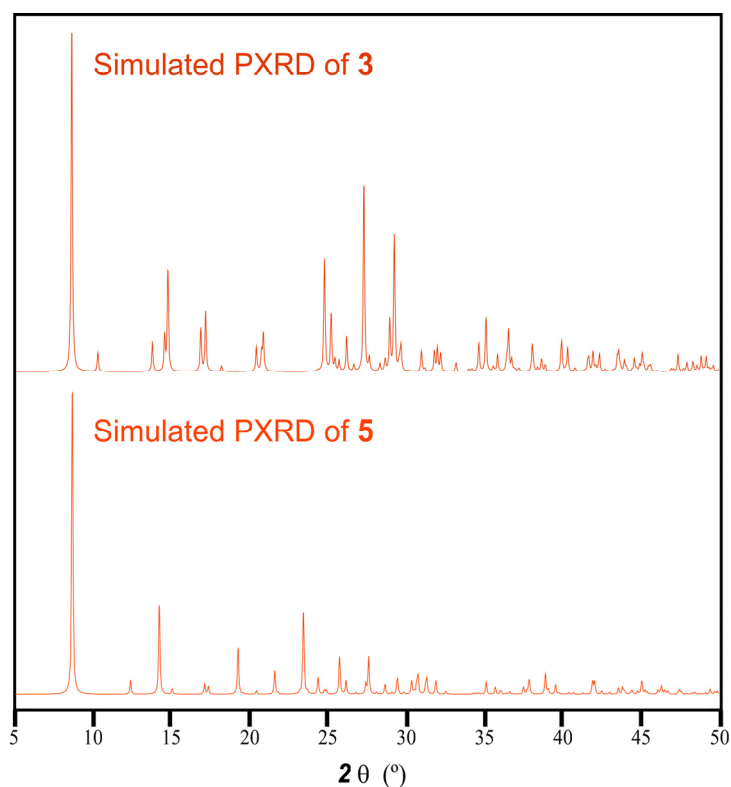


Figure S11. Comparison between PXRD data of compounds **3** and **5-DFT**.

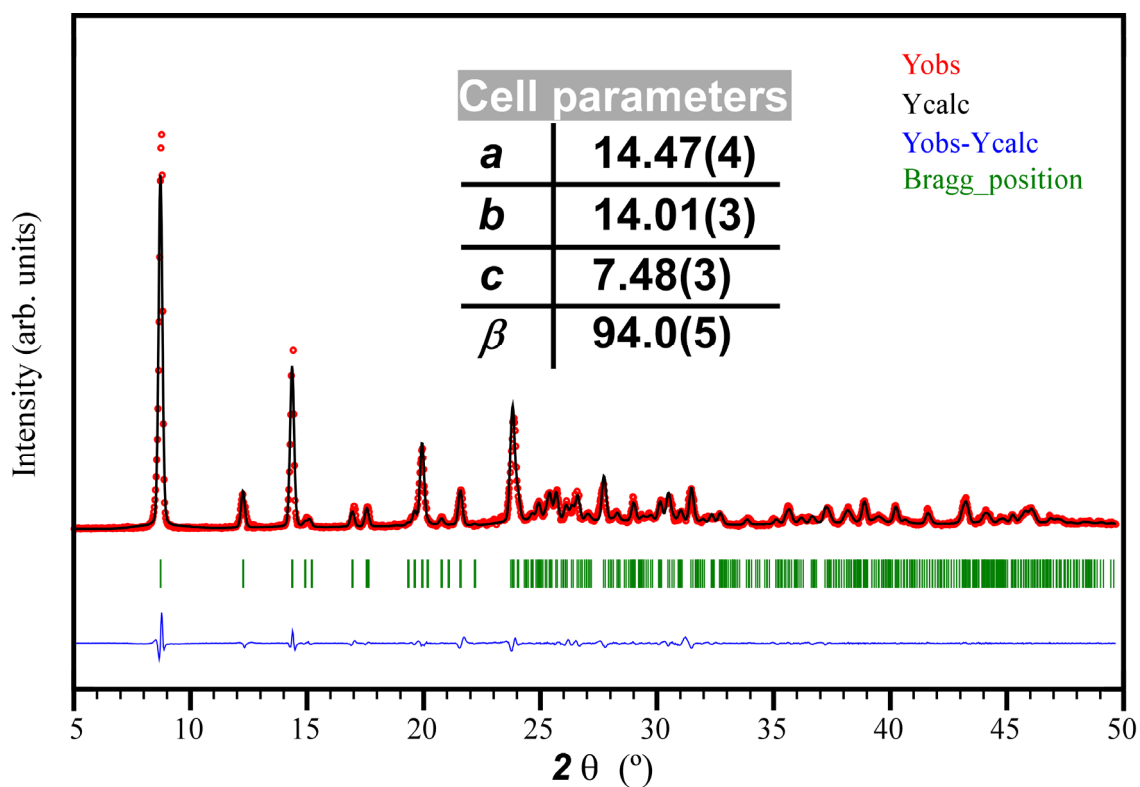


Figure S12. Pattern-matching refinement of the PXR D for compound 5.

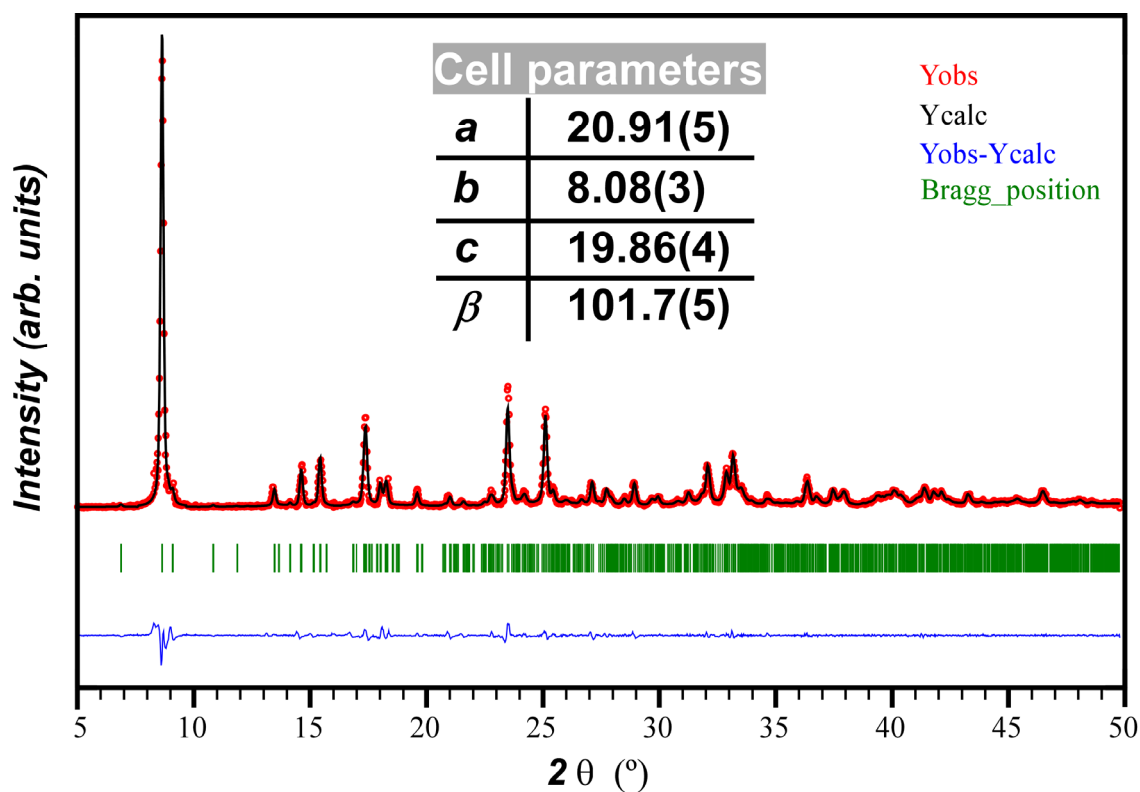


Figure S13. Pattern-matching refinement of the PXR D for compound 6.

S4. Structural details of compounds 1, 3, and 4.

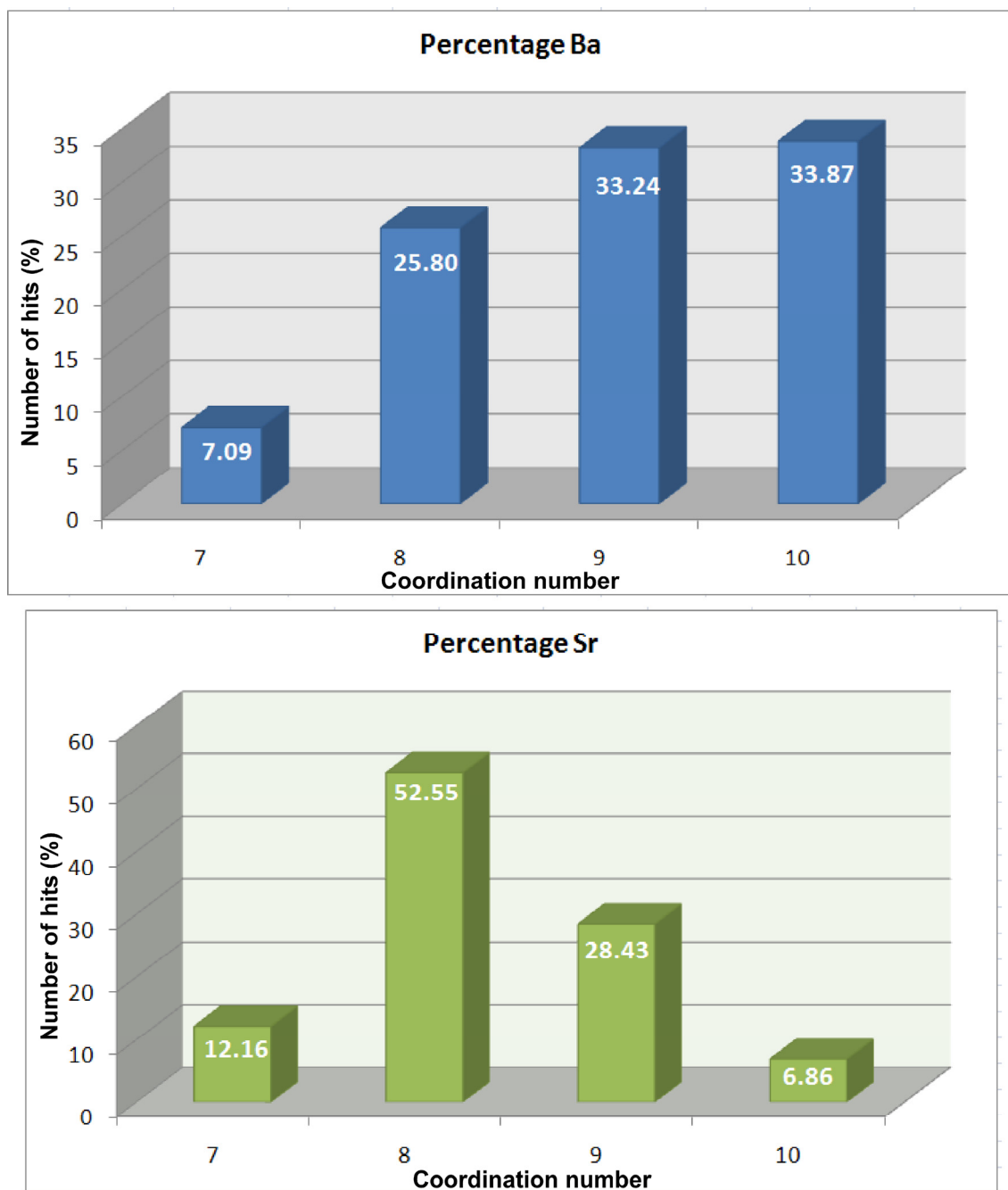


Figure S14. Appearance of most habitual coordination numbers in Ba and Sr compounds.

Table S7. Structural parameters (Å, °) of hydrogen bonds (Å, °) in compound **1**.^a

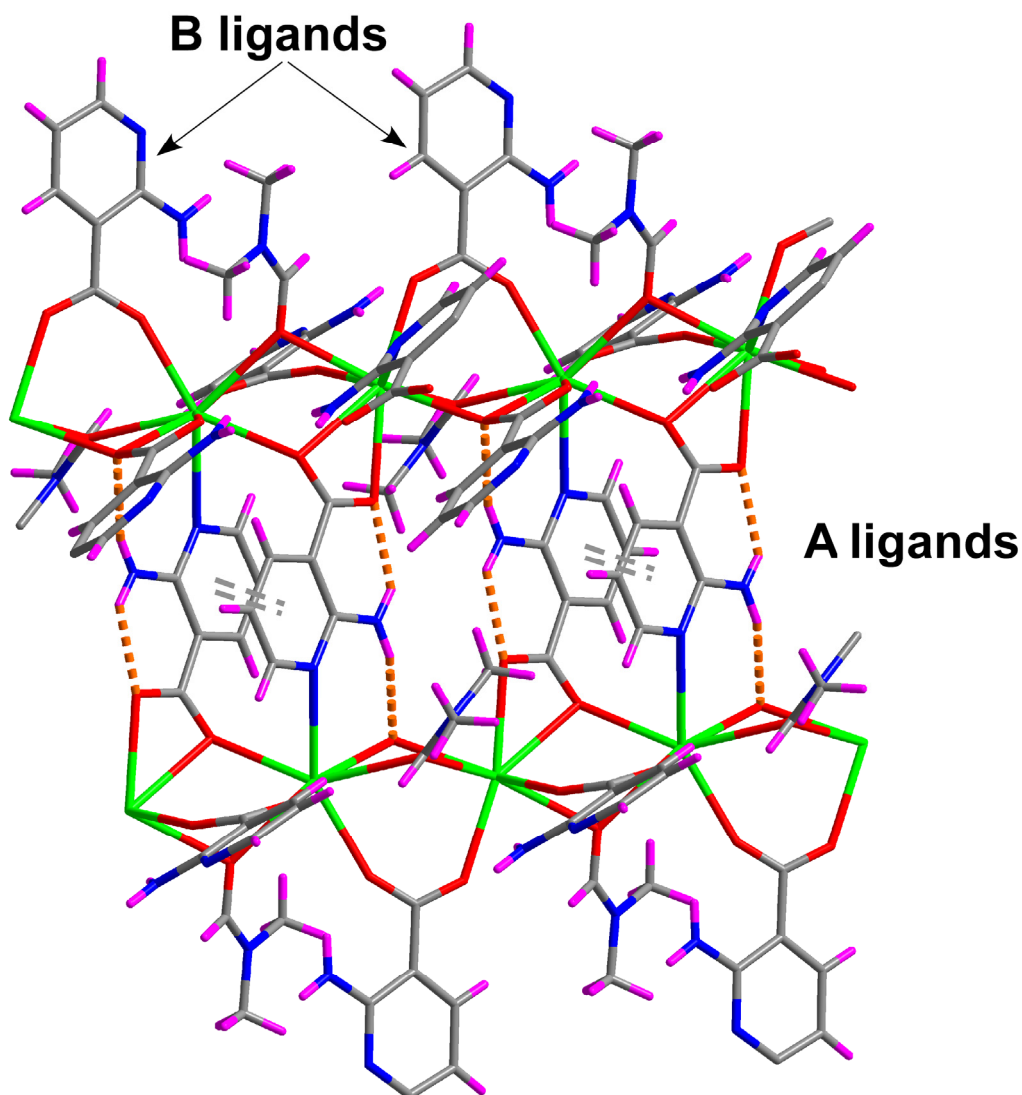
$D-H\cdots A^b$	$D-H$	$H\cdots A$	$D\cdots A$	$D-H\cdots A$
N21A-H21D \cdots O2A	0.86	2.05	2.700(4)	131.8
N21A-H21C \cdots O1A(i)	0.86	2.25	3.059(4)	156.9
N21B-H21A \cdots N1B(ii)	0.86	2.16	2.997(5)	163.9
N21B-H21B \cdots O31B	0.86	2.09	2.713(4)	128.4

^a Symmetry codes: (i) $-x + 1, y - 1/2, -z + 5/2$; (ii) $-x, -y + 1, -z + 2$. ^b D: donor. A: acceptor.

Table S8. Structural parameters (Å, °) of π - π interactions of compound **1**.^a

Ring...Ring ^b	α	DC	β	DZ	Dist.
1A-1A(iii)	0.00	3.609(2)	23.70	3.30	3.43-3.57
1B-1B(vi)	0.00	3.605(2)	23.30	3.31	3.43-3.57

[a] Symmetry: (iii) $-x + 1, -y, -z + 2$; (vi) $-x, -y + 1, -z + 1$. α : dihedral angle between mean planes of the rings (°), DC: distance between ring centroids (Å), β : angle between DC vector and normal to plane(I) (°), DZ: perpendicular distance of the centroids of ring(I) on plane of ring(II) (Å), Dist.: shorter distances between non-hydrogen atoms of rings (I) and (II). [b] Rings: **1A**: N1A, C2A, C3A, C4A, C5A, C6A; **1B**: N1B, C2B, C3B, C4B, C5B, C6B.

**Figure S15.** Hydrogen bonding (dotted orange lines) and face-to-face π - π interactions reinforcing the layer of compound **1**.

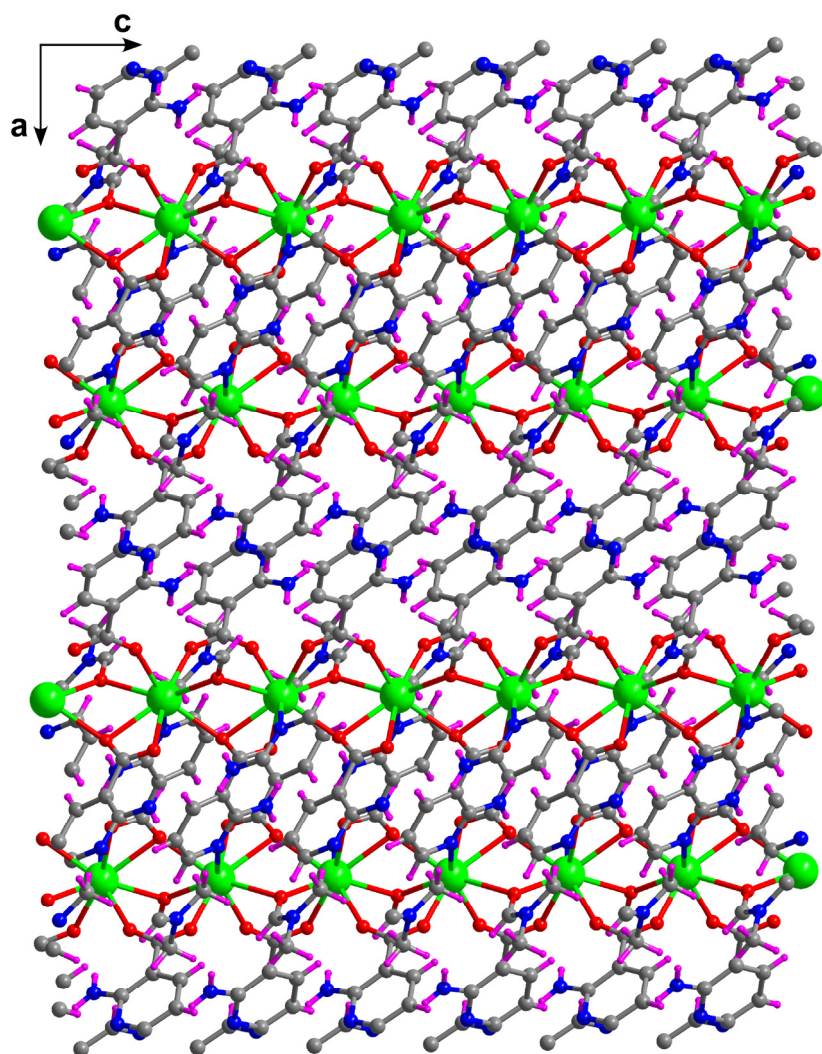


Figure S16. View of the packing of compound **1** along the crystallographic *b* axis.

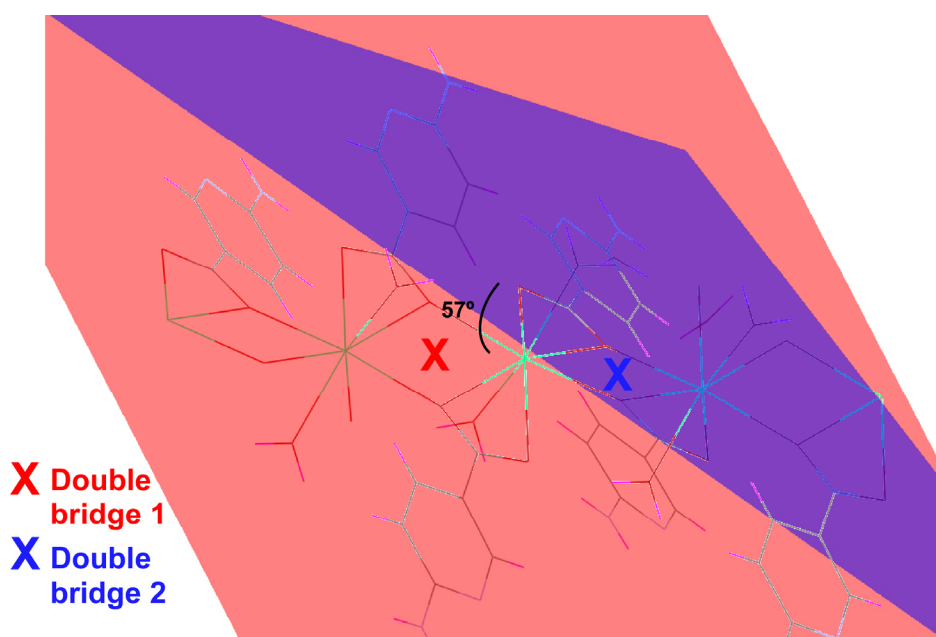


Figure S17. Angle between two successive double bridges in the chain of compound **3**.

Table S9. Structural parameters (Å, °) of hydrogen bonds (Å, °) in compound **3**.^a

$D-H\cdots A^b$	$D-H$	$H\cdots A$	$D\cdots A$	$D-H\cdots A$
O1w-H11w \cdots O2(i)	0.83	1.91	2.730(1)	166.1
O1w-H12w \cdots N1(ii)	0.87	2.09	2.960(2)	176.2
O2w-H11w \cdots O1w(iii)	0.86	2.18	3.027(2)	172.3
O2w-H22w \cdots O2w	0.85	2.00	2.810(2)	157.8
O3w-H31w \cdots O2w(iv)	0.85	2.01	2.846(2)	167.6

^a Symmetry codes: (i) $x, y, z - 1$; (ii) $-x + 3/2, -y + 1/2, -z$; (iii) $-x + 1, y, -z - 1/2$; (iv) $x, -y + 1, -z + 1/2$. ^b D: donor. A: acceptor.

Table S10. Structural parameters (Å, °) of π - π interactions of compound **3**.^a

Ring...Ring ^b	α	DC	β	DZ	Dist.
1A-1A(ii)	0.02	3.523(1)	15.16	3.40	3.51-3.54

[a] Symmetry: (ii) $-x + 3/2, -y + 1/2, -z$. α : dihedral angle between mean planes of the rings (°), DC: distance between ring centroids (Å), β : angle between DC vector and normal to plane(I) (°), DZ: perpendicular distance of the centroids of ring(I) on plane of ring(II) (Å), Dist.: shorter distances between non-hydrogen atoms of rings (I) and (II). [b] Rings: 1A: N1, C2, C3, C4, C5, C6.

Table S11. Parameters (Å, °) for hydrogen bonding and π - π interactions for the DFT computed structure of compound **5**.^a

$D-H\cdots A^b$	$D-H$	$H\cdots A$	$D\cdots A$	$D-H\cdots A$	
O1w-H11w \cdots O2(i)	0.83	1.91	2.730(1)	166.1	
O1w-H12w \cdots N1(ii)	0.87	2.09	2.960(2)	176.2	
O2w-H11w \cdots O1w(iii)	0.86	2.18	3.027(2)	172.3	
Ring...Ring ^b	α	DC	β	DZ	Dist.
1A-1A(ii)	0.02	3.523(1)	15.16	3.40	3.51-3.54

^a Symmetry codes: (i) $x, y, z - 1$; (ii) $-x + 3/2, -y + 1/2, -z$; (iii) $-x + 1, y, -z - 1/2$; (iv) $x, -y + 1, -z + 1/2$. ^b D: donor. A: acceptor.

The transformation of **3** to **5** promotes the shrinkage of the structure associated with the loss of the crystallization water molecules (three water molecules per formula unit) present in compound **3**, because compound **5** contains no crystallization water molecules. As a result, microchannels occupied by crystallization water molecules in **3** disappear and permit the rearrangement of 6ani ligands pending from the 1D structure.

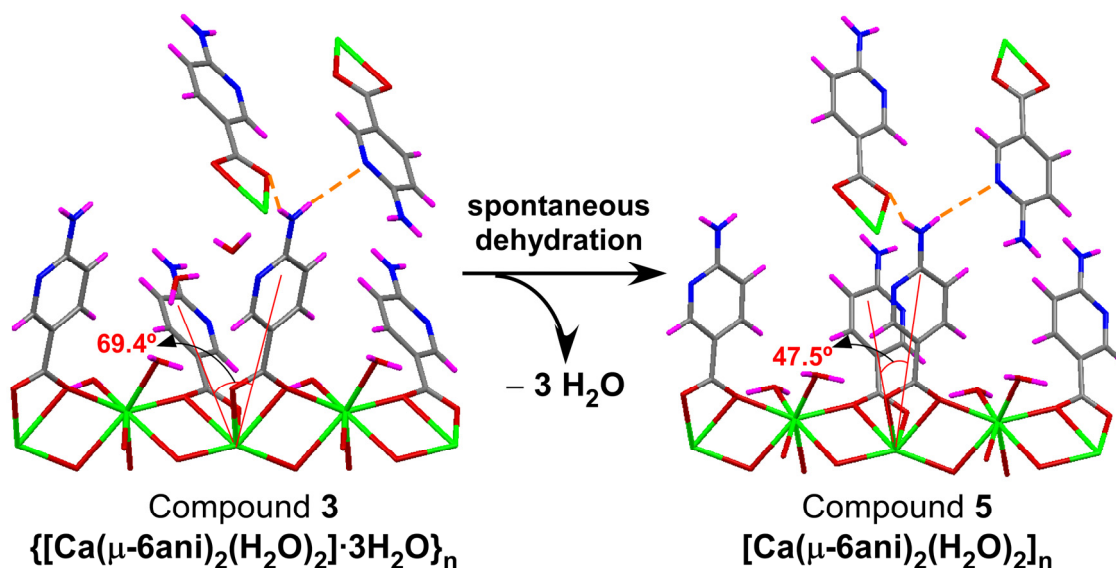


Figure S18. Main structural differences occurring at the crystal structure upon the spontaneous dehydration of compound **3** to yield compound **5**. Note that supramolecular hydrogen bonds (drawn by dotted orange lines) are maintained during the dehydration.

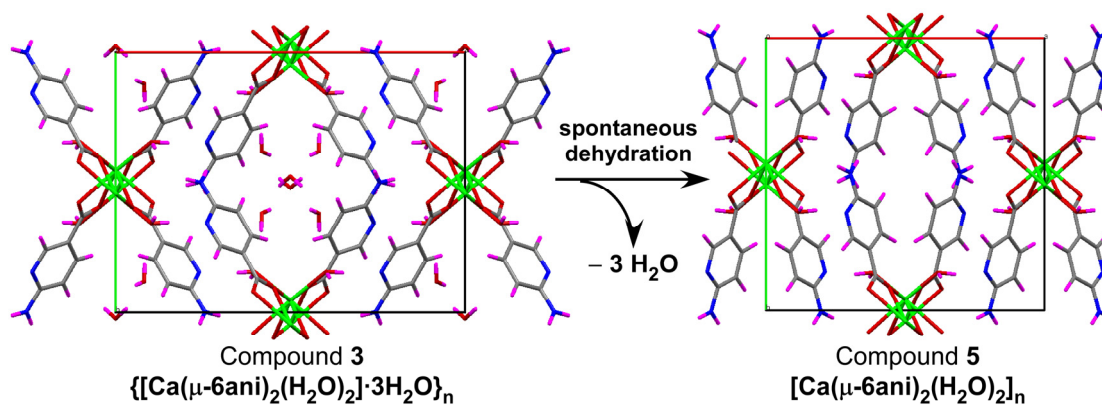


Figure S19. Packing views of the crystal structure during the **3** \rightarrow **5** dehydration.

S5. Diffuse reflectance results for compounds 1, 2, 4, 5 and 6.

The diffuse reflectance spectra were converted into Tauc plots by applying the Kubelka-Munk function and employed to estimate the optical band gaps of the compounds.

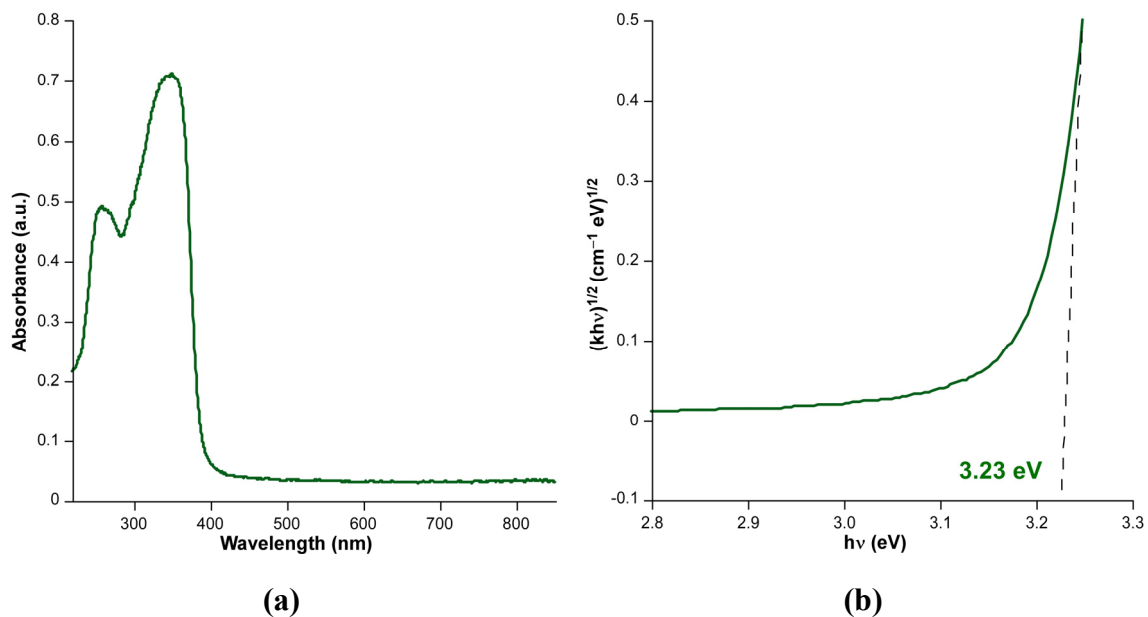


Figure S20. Diffuse reflectance data for compound 1: (a) plotted as solid-state absorption, (b) Tauc plot showing the estimated band gap.

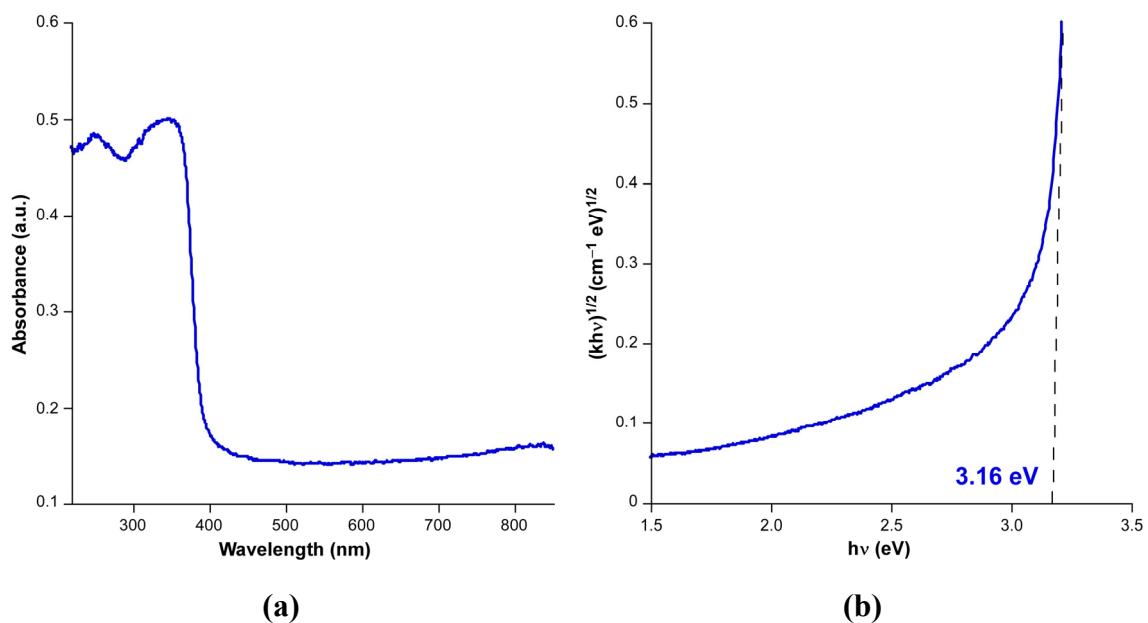
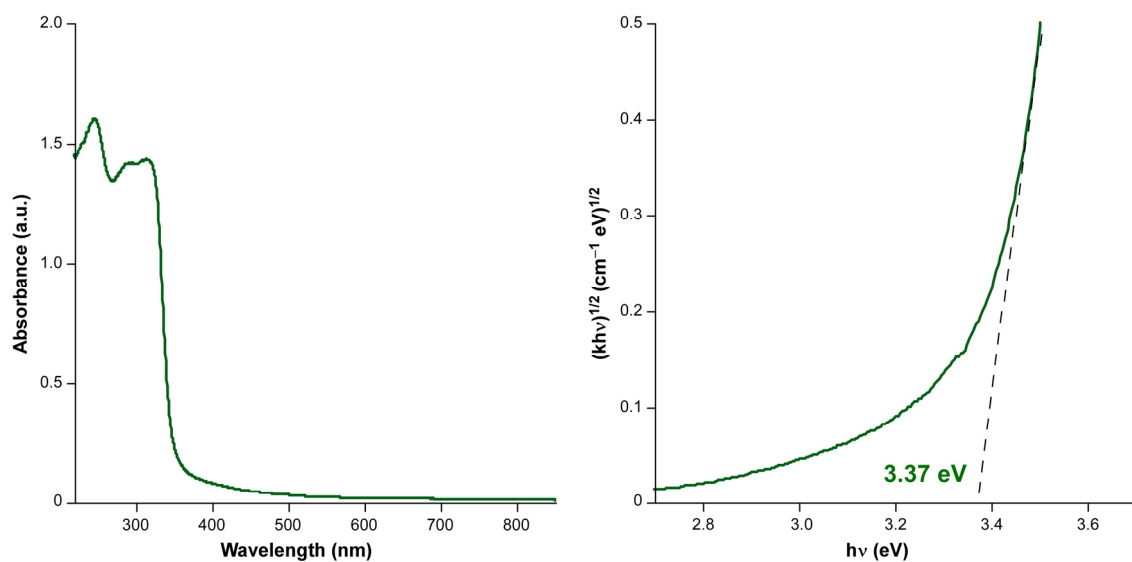


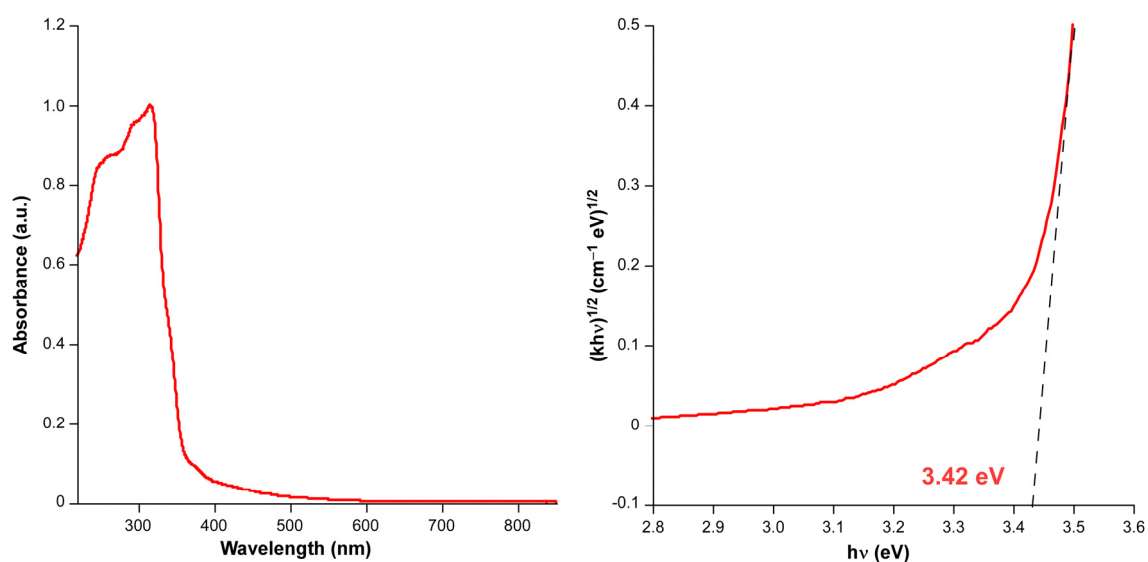
Figure S21. Diffuse reflectance data for compound 2: (a) plotted as solid-state absorption, (b) Tauc plot showing the estimated band gap.



(a)

(b)

Figure S22. Diffuse reflectance data for compound 4: (a) plotted as solid-state absorption, (b) Tauc plot showing the estimated band gap.



(a)

(b)

Figure S23. Diffuse reflectance data for compound 5: (a) plotted as solid-state absorption, (b) Tauc plot showing the estimated band gap.

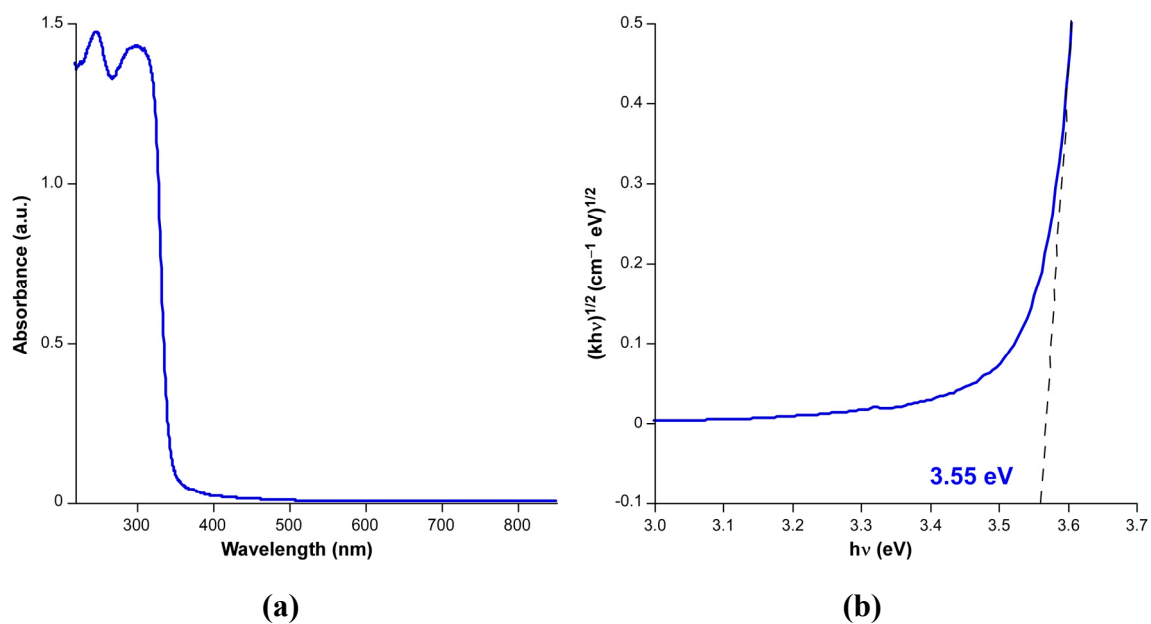


Figure S24. Diffuse reflectance data for compound **6**: (a) plotted as solid-state absorption, (b) Tauc plot showing the estimated band gap.

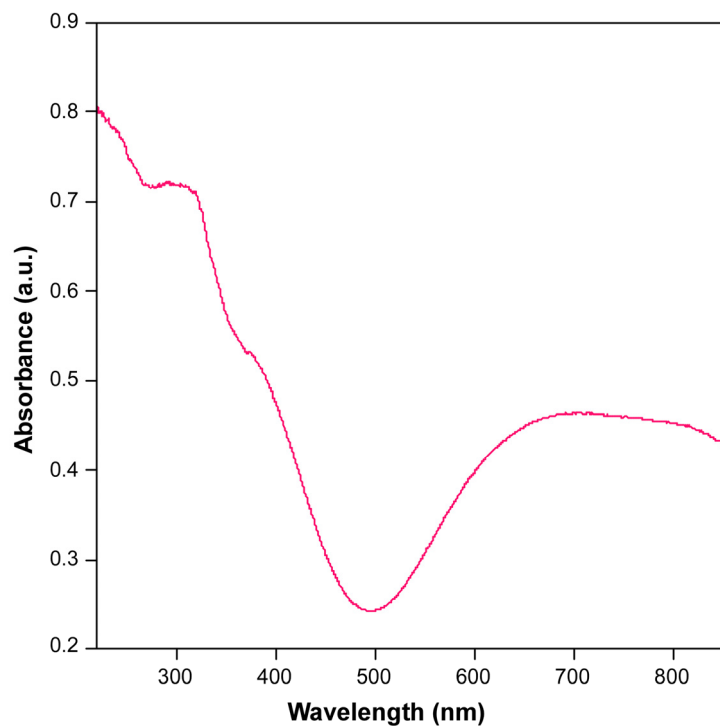


Figure S25. Diffuse reflectance data for compound **4** after Cu^{2+} have been exchanged, showing the typical d-d transition for the transition metal ion.

S6. Band gap calculation by means of periodic density of states.

Band gap was estimated for those compounds whose crystal structures have been solved by X-ray diffraction.

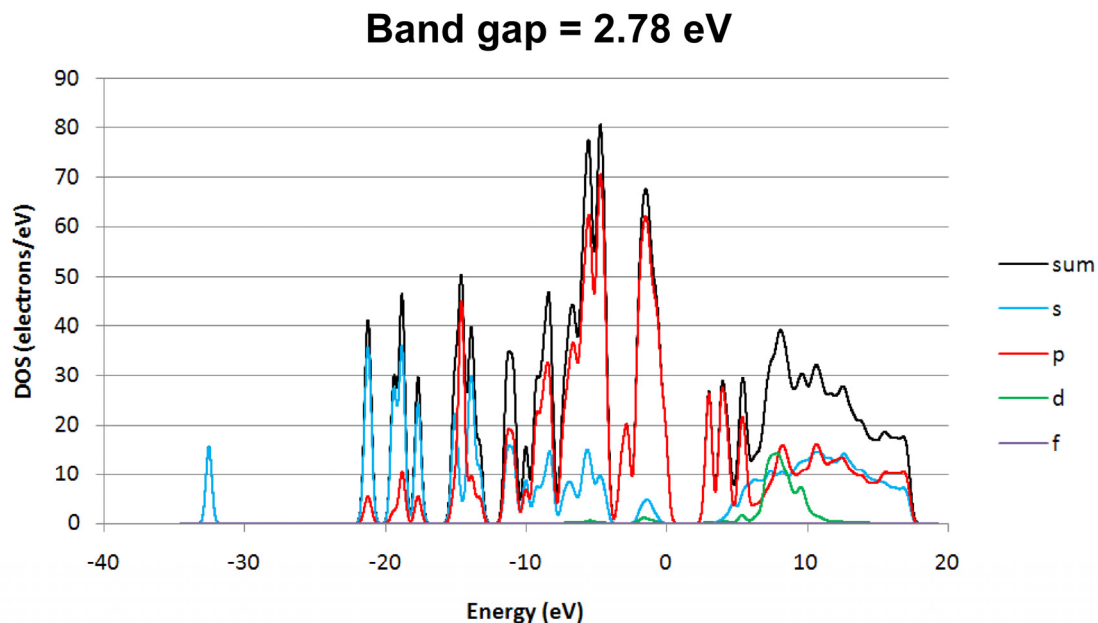


Figure S26. Partial (PDOS) and total (TDOS) electronic density of states showing the contribution of each sort of orbital for compound 1.

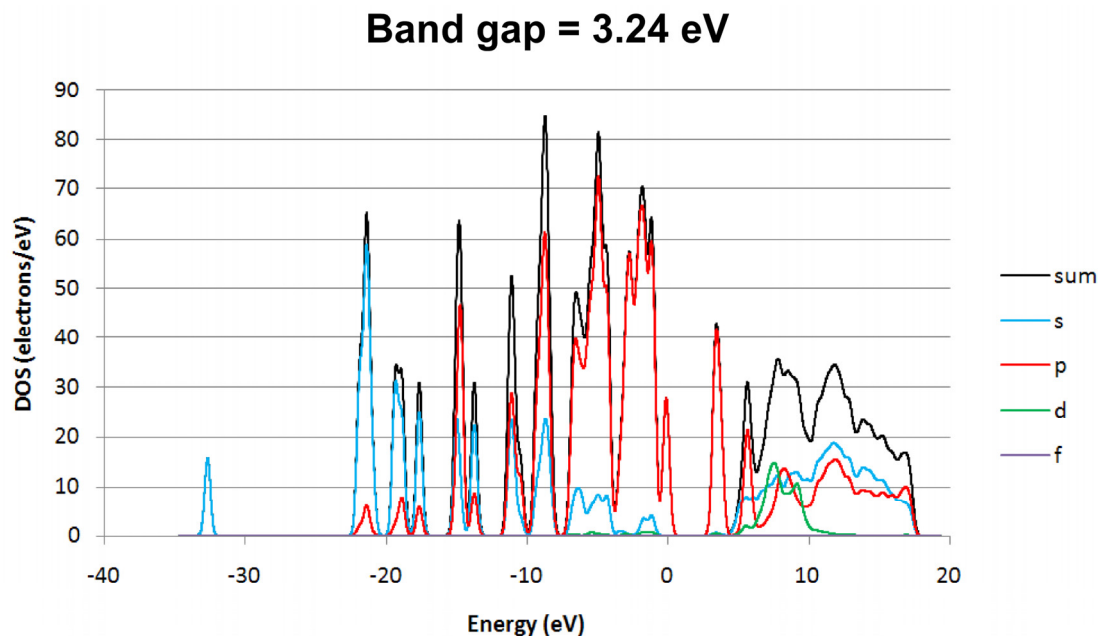


Figure S27. Partial (PDOS) and total (TDOS) electronic density of states showing the contribution of each sort of orbital for compound 4.

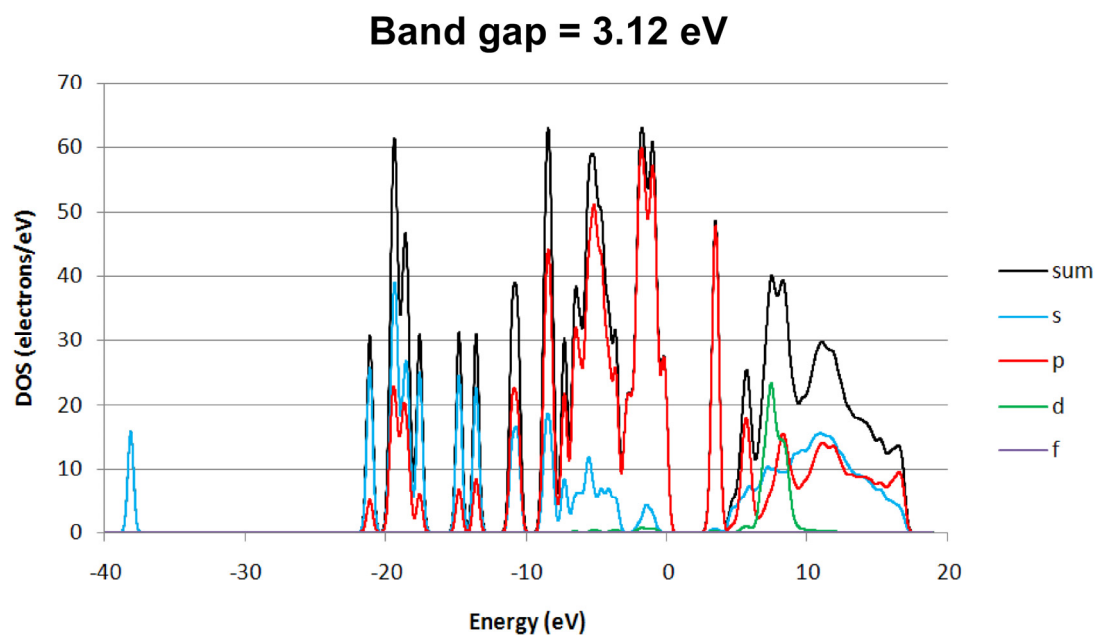


Figure S28. Partial (PDOS) and total (TDOS) electronic density of states showing the contribution of each sort of orbital for the optimized structure of compound **5**.

Table S12. Comparative values of band gap estimated from experimental diffuse reflectance data and periodic DOS (eV).

Compounds	Experimental (diffuse reflectance)	Theoretical (periodic DOS)
1	3.23	2.78
2	3.16	–
4	3.37	3.24
5	3.42	3.12
6	3.45	–

S7. Photoluminescence measurements.

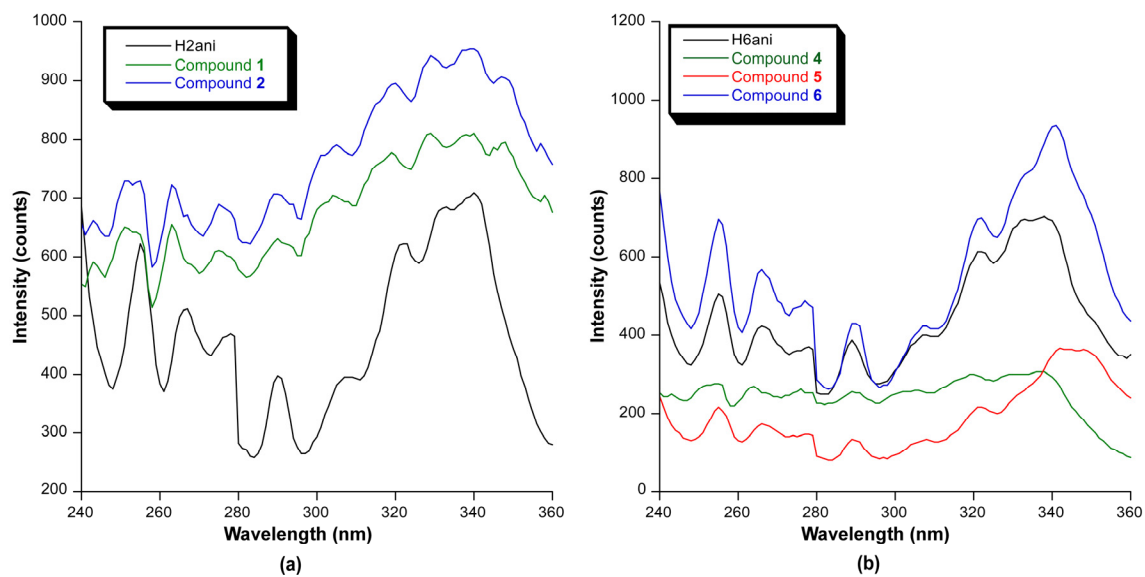


Figure S29. Excitation spectra of all compounds at room temperature compared to their relatives: **(a)** H2ani and compounds **1** and **2**; **(b)** H6ani and compounds **4**, **5** and **6** monitoring their maximum emission wavelength.

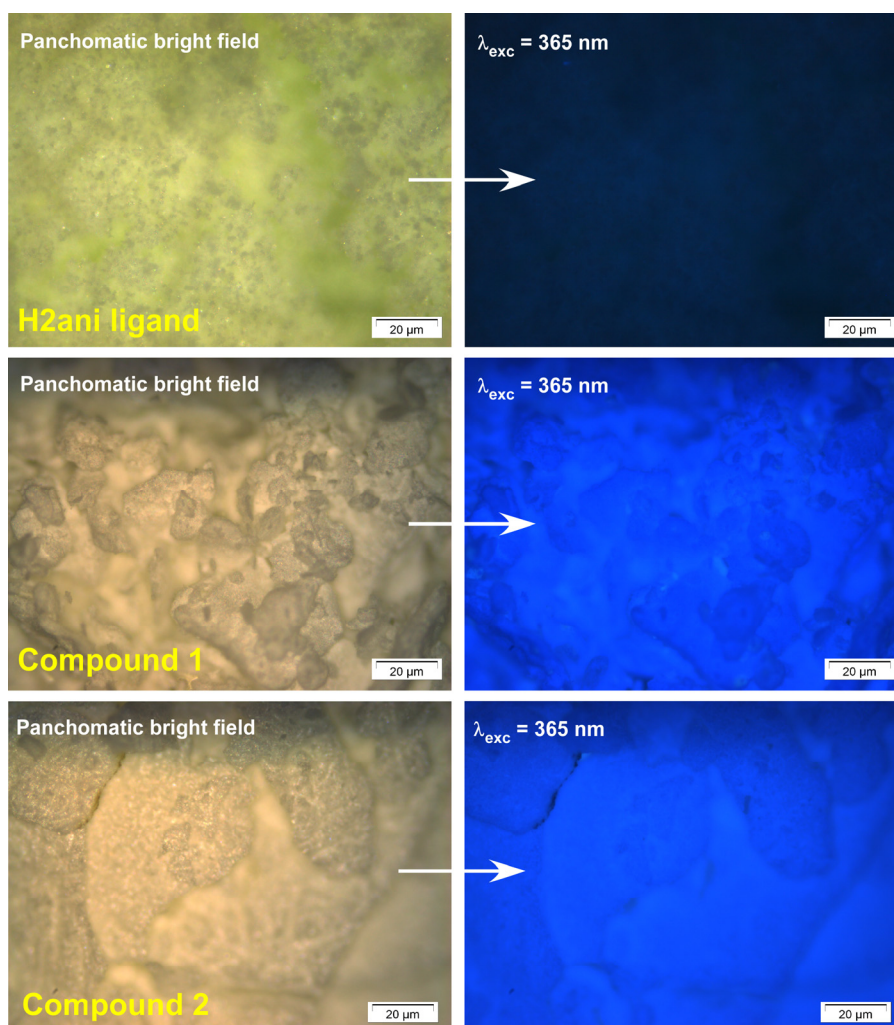


Figure S30. Comparison of micro-PL images taken on H2ani ligand and compounds **1** and **2** under panchromatic field and UV radiation.

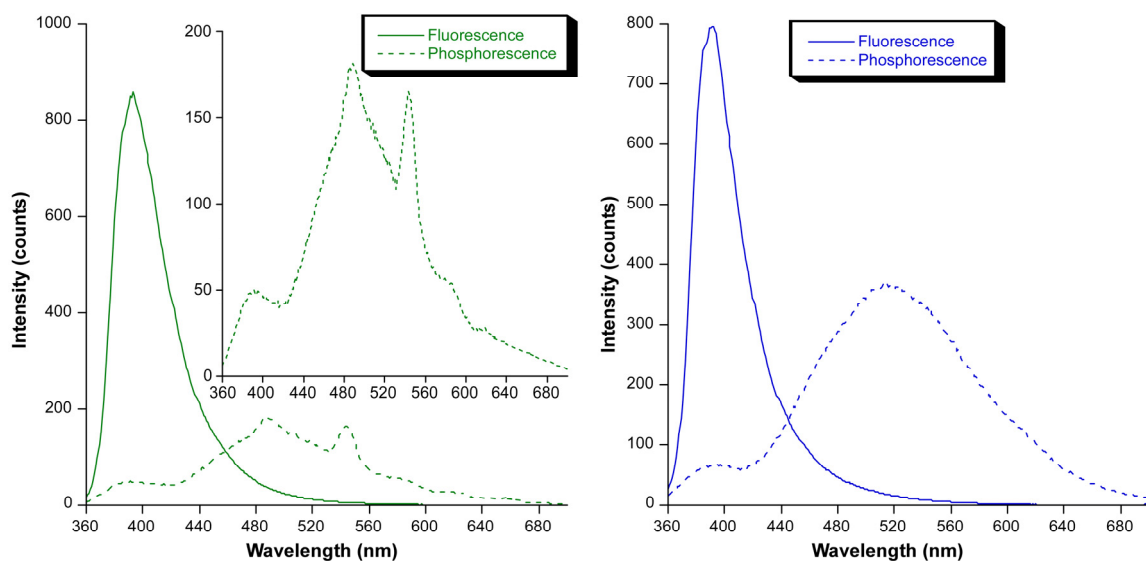


Figure S31. Room temperature emission fluorescence and phosphorescence spectra of compounds **1** (left) and **2** (right).

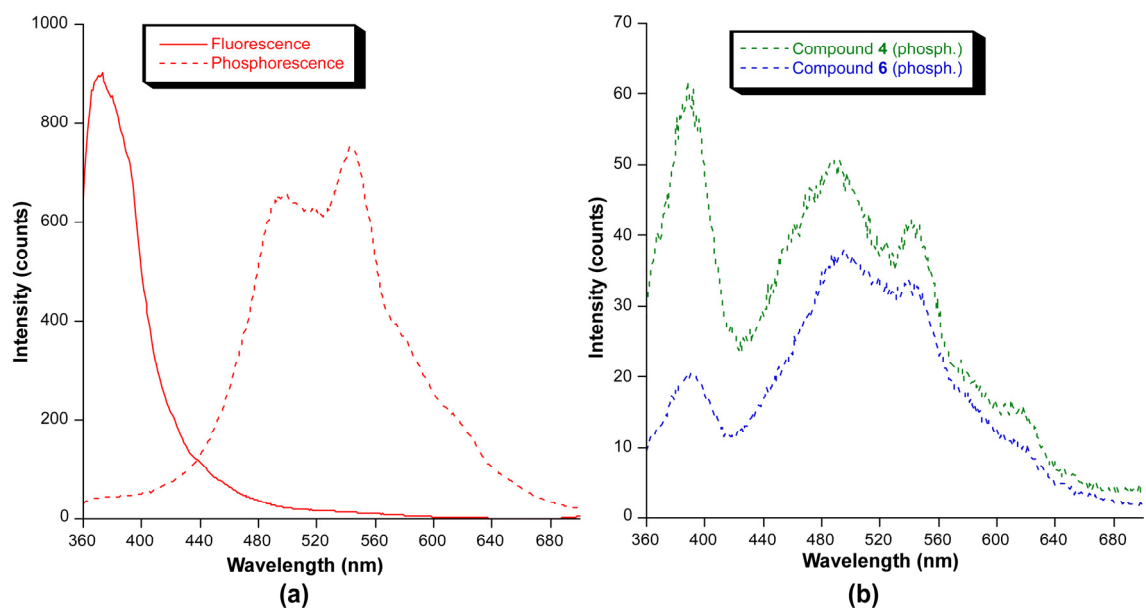


Figure S32. (a) Emission fluorescence and phosphorescence spectra for compound **5**. (b) Phosphorescence spectra of compounds **4** and **6**.

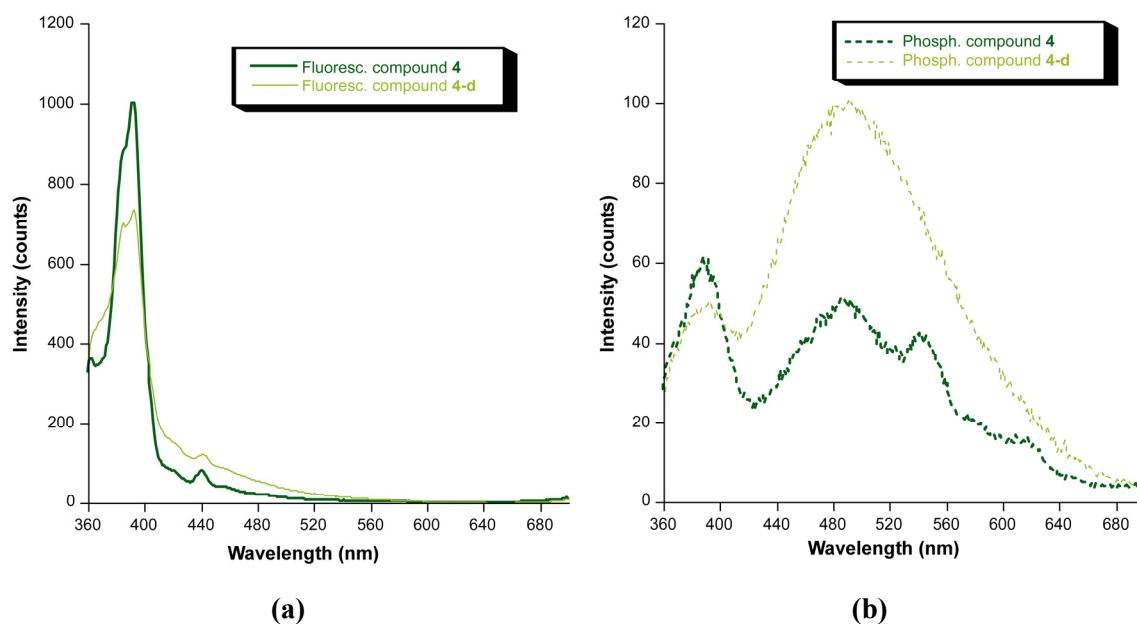


Figure S33. Comparison of the photoluminescence emission for compounds **4** and **4-d**: **(a)** fluorescence and **(b)** phosphorescence.

Taking compound **5** as a reference, we explored the excitation spectra at different emission wavelengths (i.e. at 386 and 450 nm involving fluorescent and phosphorescent emissions). As shown in Figure S34, a very similar pattern with excitation maxima at ca. 323 nm is obtained in both cases, which confirms that all emissions are correctly excited under 325 nm wavelength.

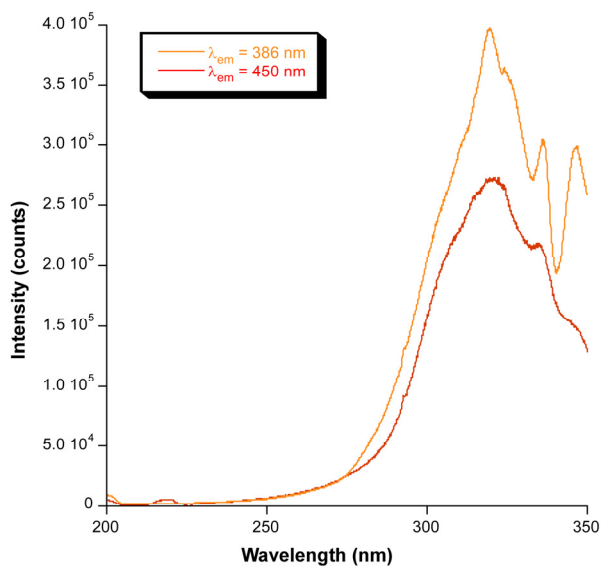


Figure S34. Low temperature (10 K) excitation spectra of compound **5** at selected emission maxima.

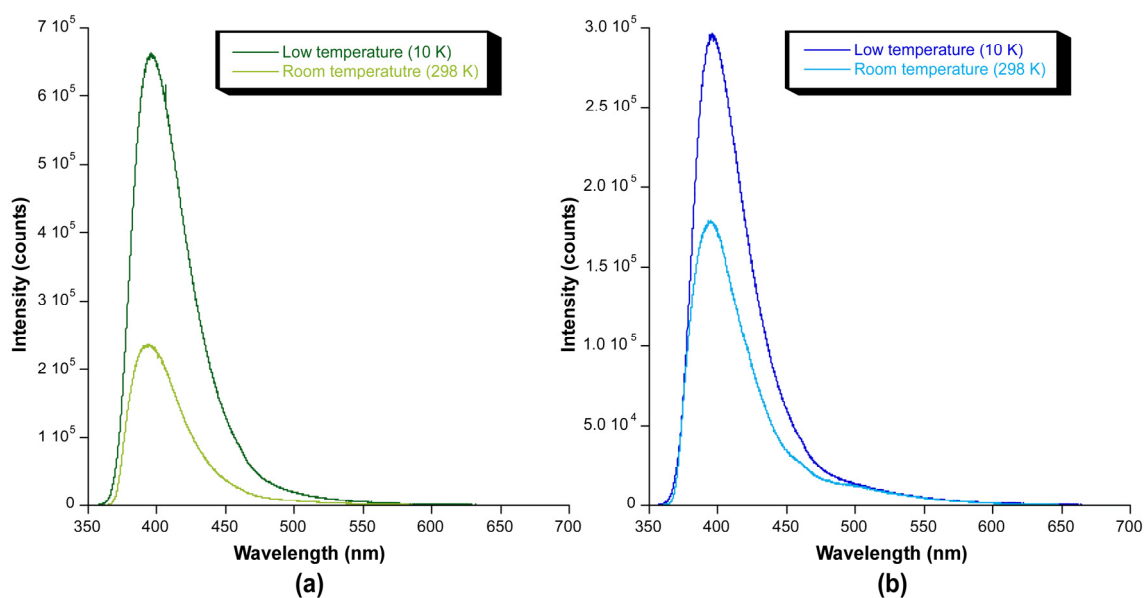


Figure S35. Comparative steady state emission at room (298 K) and low (10 K) temperature for compounds: **(a) 1** and **(b) 2** excited at 325 nm wavelength.

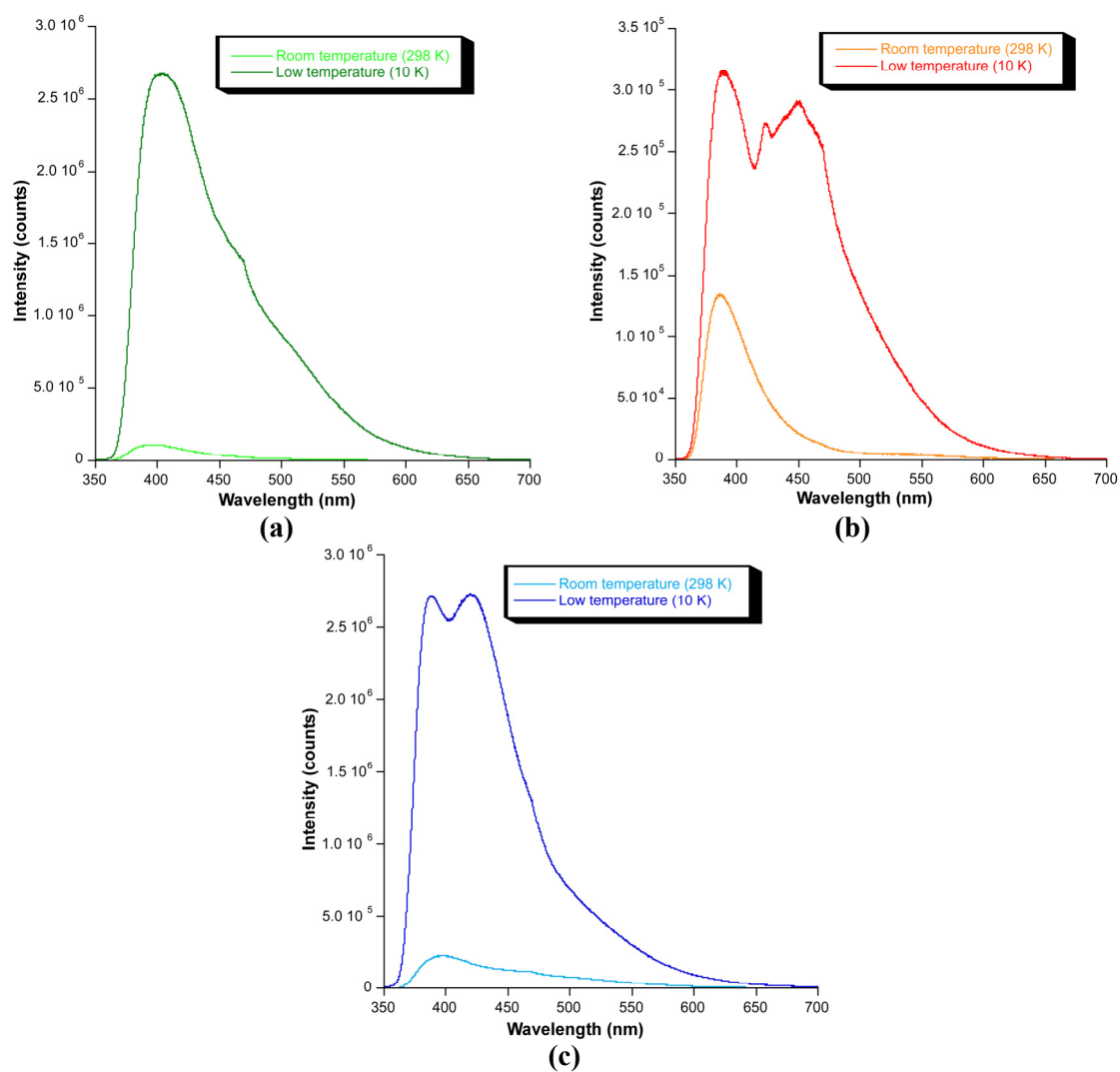


Figure S36. Comparative steady state emission at room (298 K) and low (10 K) temperature for compounds: **(a) 4**, **(b) 5** and **(c) 6** excited at 325 nm wavelength.

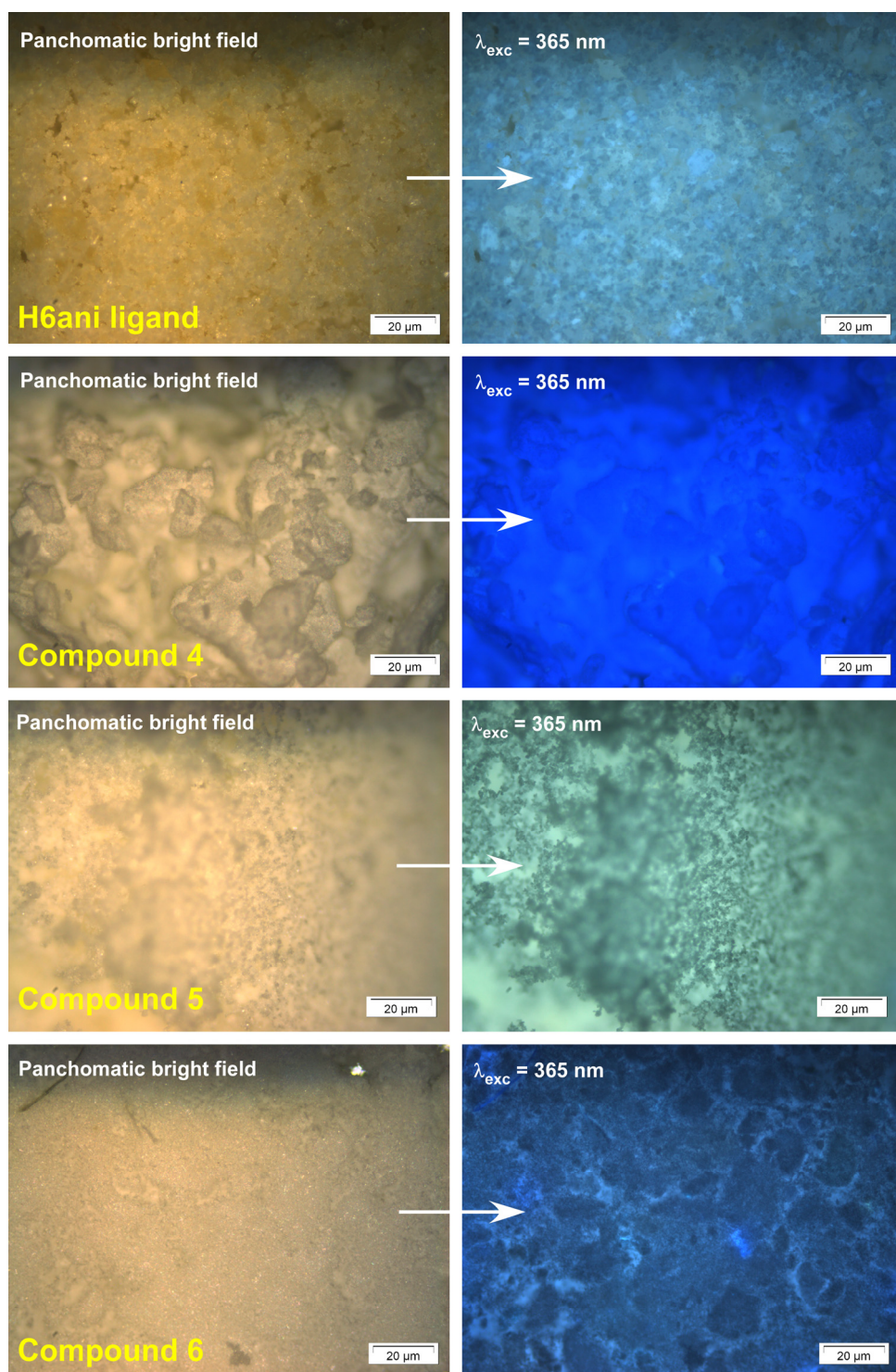


Figure S37. Comparison of micro-PL images taken on H6ani ligand and compounds 4, 5 and 6 under panchromatic field and UV radiation.

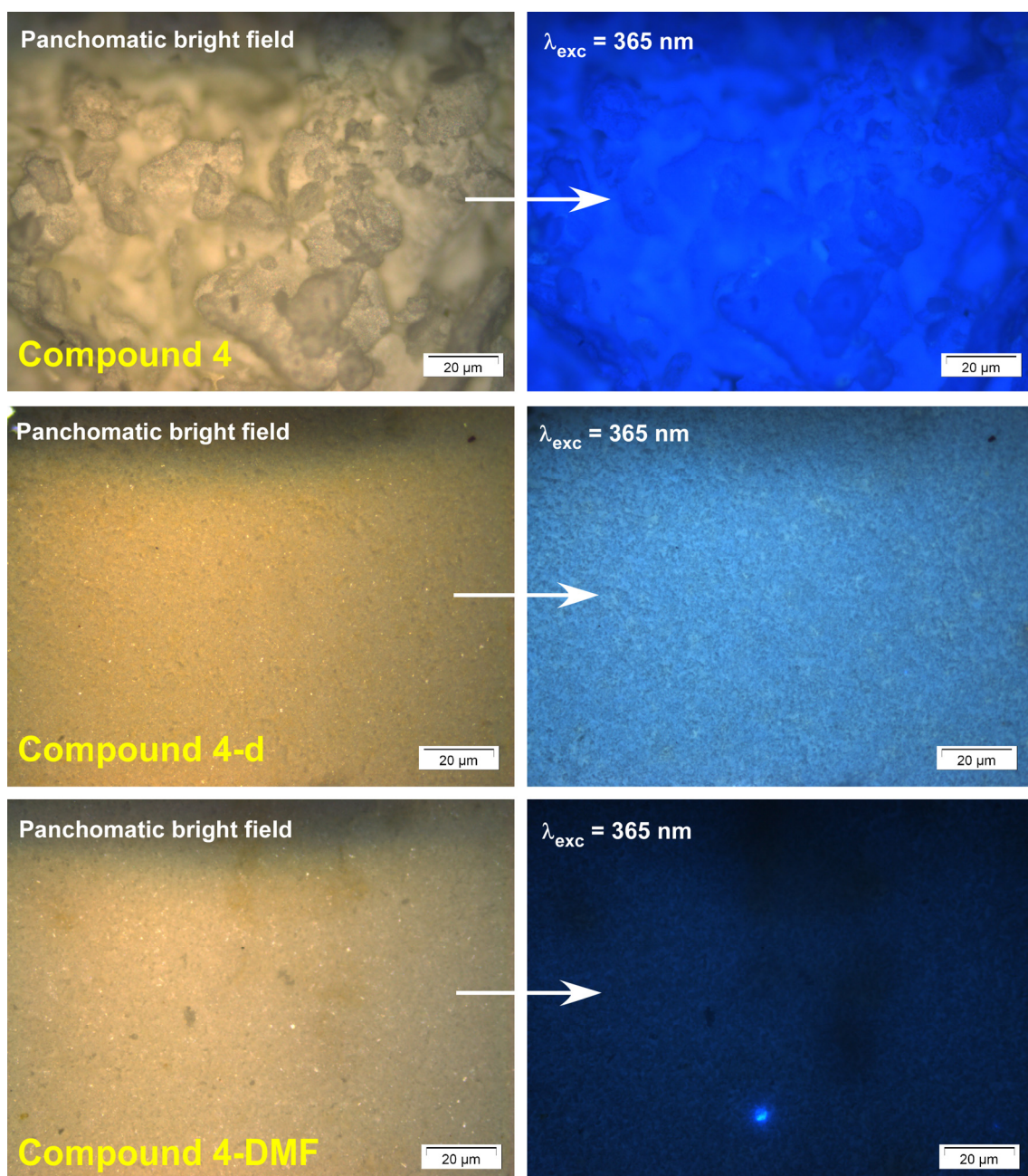


Figure S38. Comparative micro-PL images taken on compounds 4, 4-d and 4-DMF under panchromatic field and UV radiation.

S8. Lifetime measurements.

The phosphorescence properties were also measured for H2ani and H6ani ligands for comparative purposes. While at room temperature they exhibit no phosphorescence, upon cooling to 10 K they show a sizeable phosphorescence which, compared to that exhibited by AE-based compounds, is weak and short ($\tau = 97$ ms at $\lambda_{em} = 520$ nm for H2ani and $\tau = 173$ ms at $\lambda_{em} = 480$ nm for H6ani).

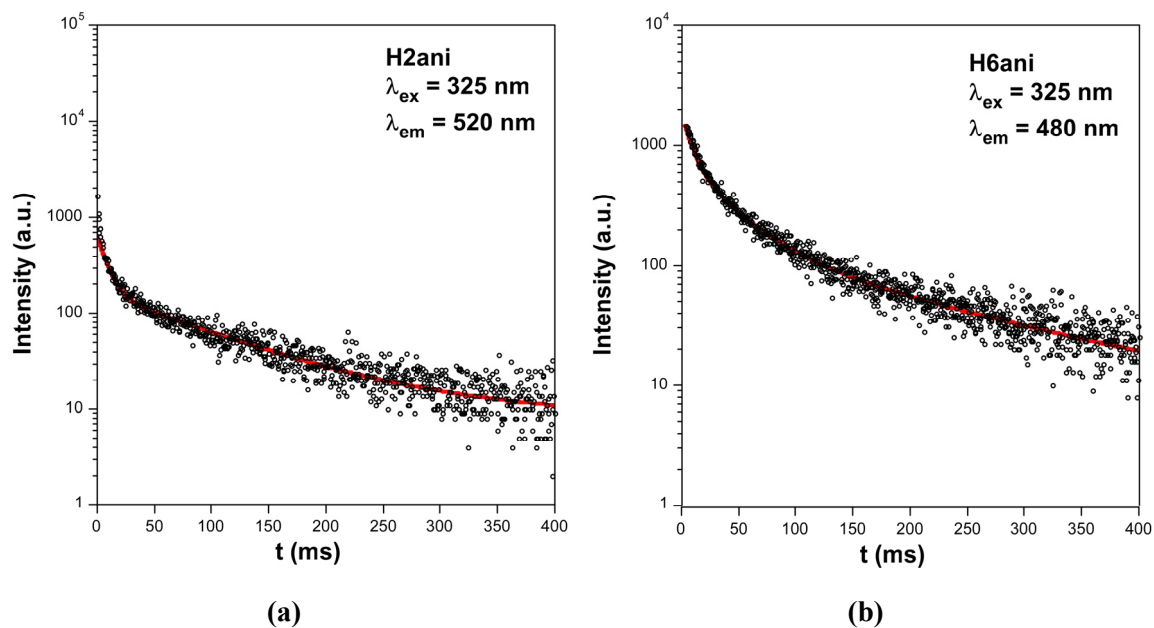
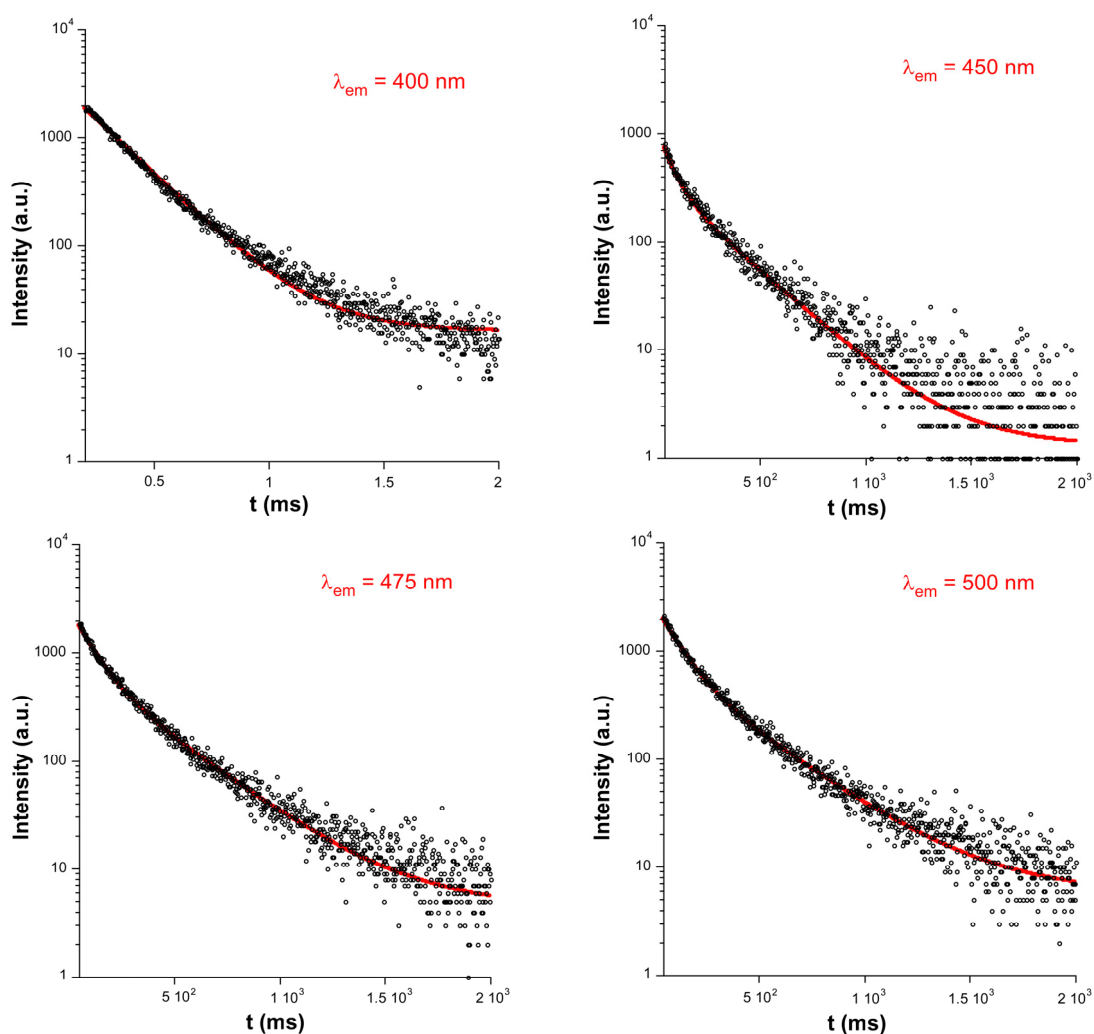


Figure S39. Fitted decay curves of H2ani and H6ani ligands at 10 K.

Lifetime measurements were performed at 10 K using polycrystalline samples under excitation at 325 nm for some selected emission wavelengths (one each *ca.* 25 nm) and covering the whole emission spectrum (in the 400–650 nm). The decay curves were recorded employing a fixed exposure time of 10 minutes but different gate times depending on the nature of the emissions (fluorescence or phosphorescence). The curves were analyzed by tail fitting using two or three lifetimes in order to reproduce fairly the non-linear distribution. Figures S40 and S41 gather all fitted decay curves while data containing the lifetimes can be found in Table S13.



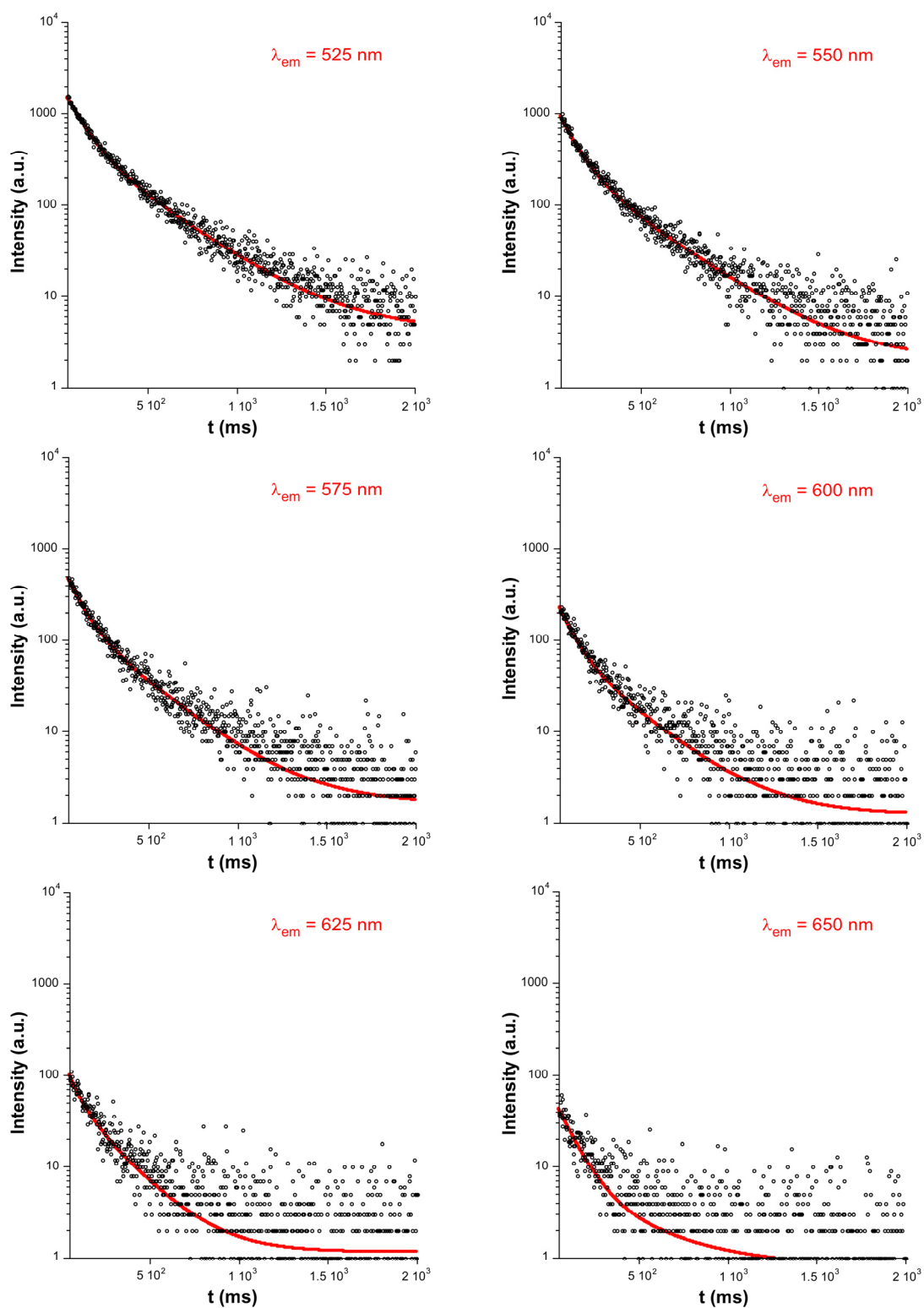
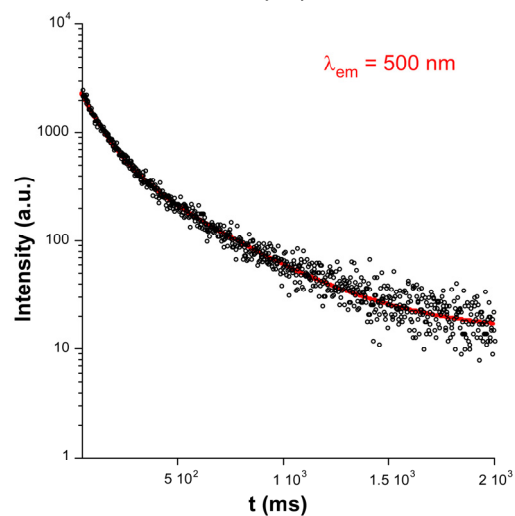
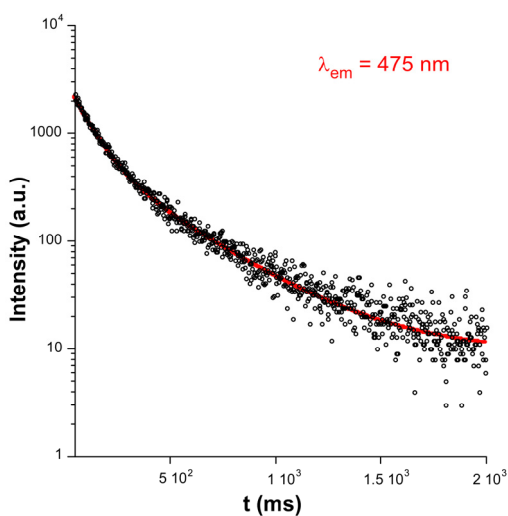
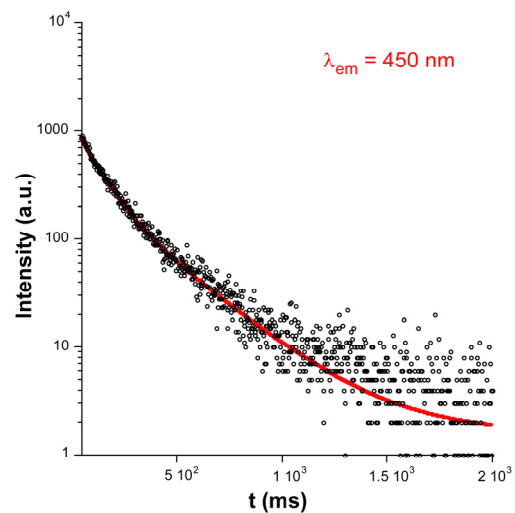
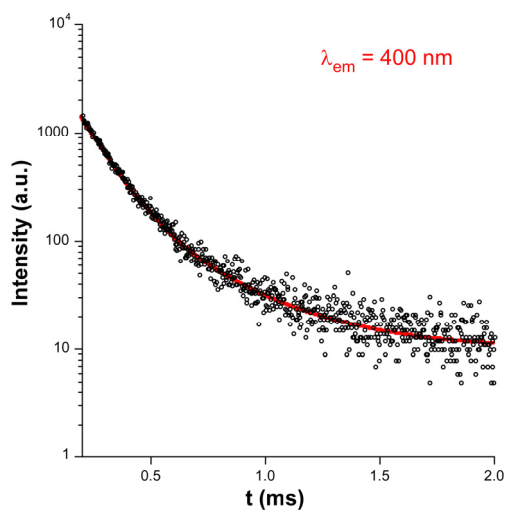


Figure S40. Emission decay curves for compound **1** at selected emission wavelength (every 25 nm in the 400–600 nm range) showing the best fitting.



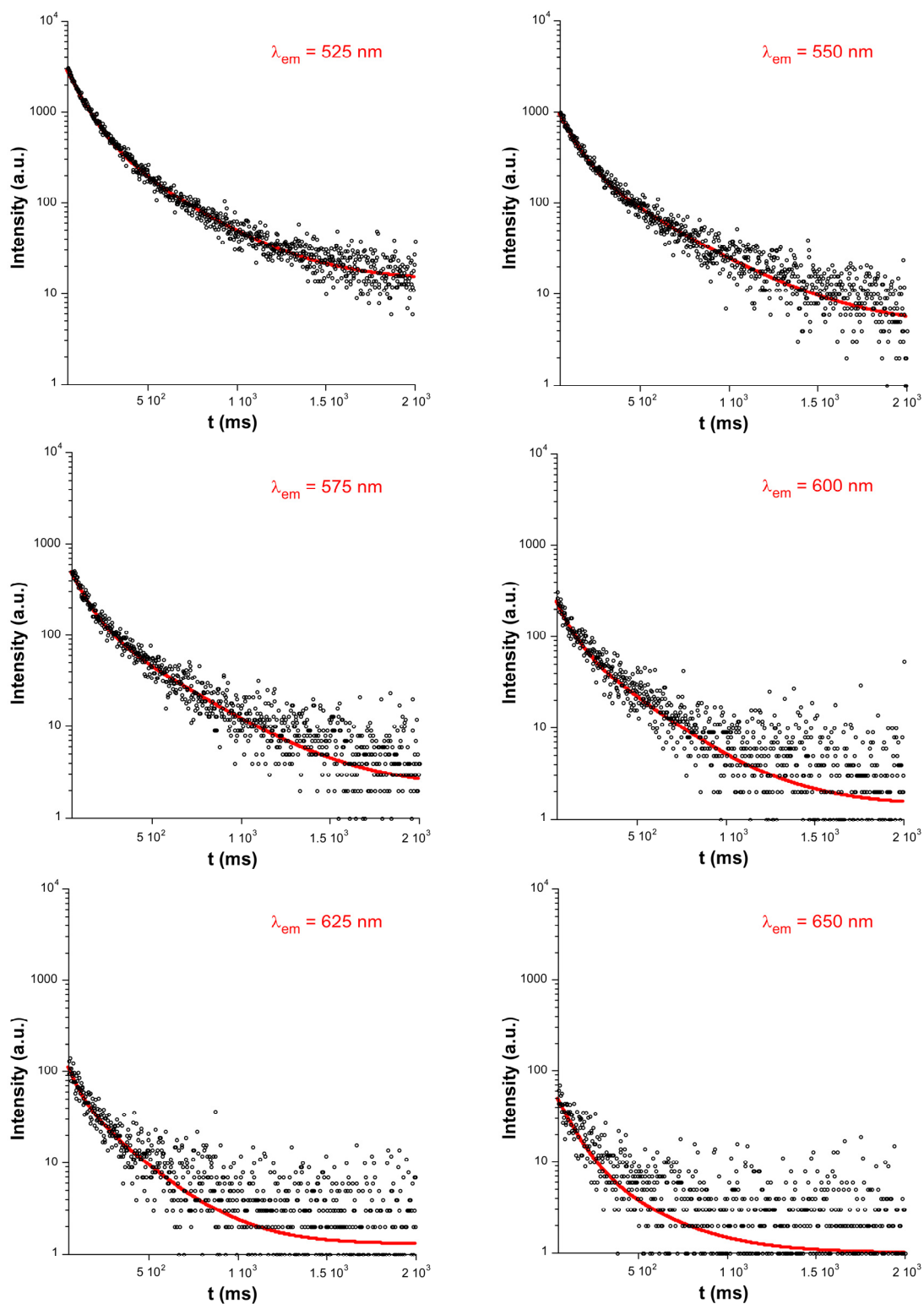


Figure S41. Emission decay curves for compound **2** at selected emission wavelength (every 25 nm in the 450–650 nm range) showing the best fitting.

Table S13. Values of lifetimes for compounds **1** and **2** estimated from best fitting of decay curves measured at 10 K accompanied by percentages for the components ($\lambda_{\text{ex}} = 340$ nm; $\lambda_{\text{em}} = 400\text{--}600$ nm).

Fluorescence emission			
$\lambda(\text{nm})$	τ_1 (μs)		Chi Sq.
Compound 1			
400	213(3) / 100%		1.152
Compound 2			
400	188(2) / 100%		1.102
Phosphorescence emission			
$\lambda(\text{nm})$	τ_1 (ms)	τ_2 (ms)	Chi Sq.
Compound 1			
450	59(1) / 23%	249(2) / 77%	1.214
475	92(1) / 33%	303(2) / 67%	1.153
500	93(1) / 41%	324(4) / 59%	1.128
525	96(1) / 40%	319(3) / 60%	1.162
550	100(1) / 38%	317(2) / 62%	1.117
575	82(2) / 36%	285(4) / 64%	1.221
600	79(3) / 35%	273(6) / 65%	1.154
625	63(5) / 23%	210(6) / 77%	1.126
650	99(5) / 65%	170(2) / 35%	1.250
Compound 2			
450	97(2) / 42%	282(4) / 58%	1.137
475	94(3) / 42%	345(3) / 58%	1.116
500	92(1) / 39%	357(3) / 61%	1.158
525	93(1) / 49%	325(3) / 51%	1.128
550	91(1) / 38%	369(4) / 62%	1.154
575	85(2) / 36%	351(5) / 64%	1.176
600	76(3) / 30%	299(5) / 70%	1.133
625	63(4) / 24%	249(6) / 76%	1.179
650	92(6) / 50%	216(7) / 50%	1.215

Lifetime measurements of compounds **4**, **5** and **6** were measured under similar experimental conditions (Figure S42–44). Compound **4** does not show persistent emission above 525 nm. Moreover, only three selected emission wavelengths have been explored for compound **6** due to its weak emission (see Table S14).

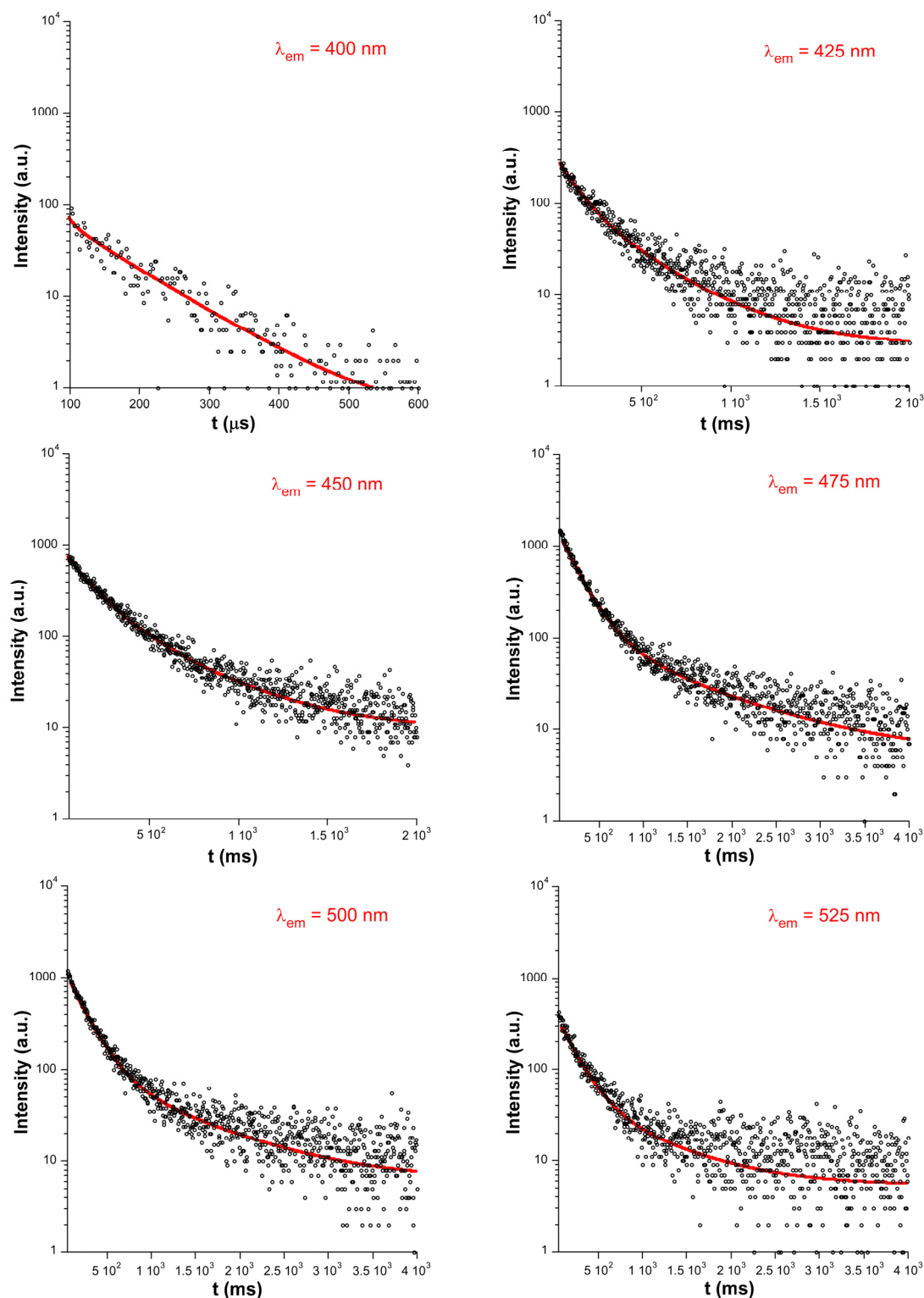
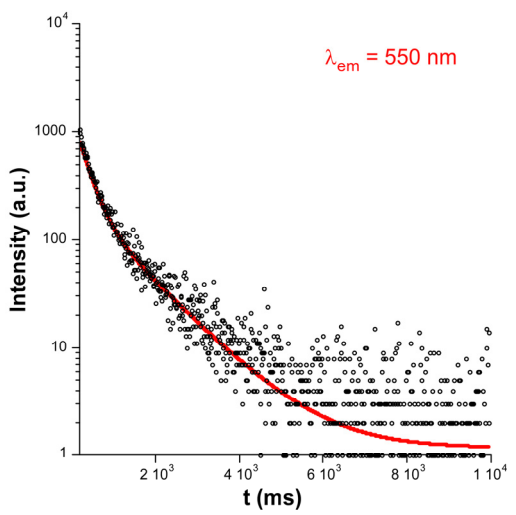
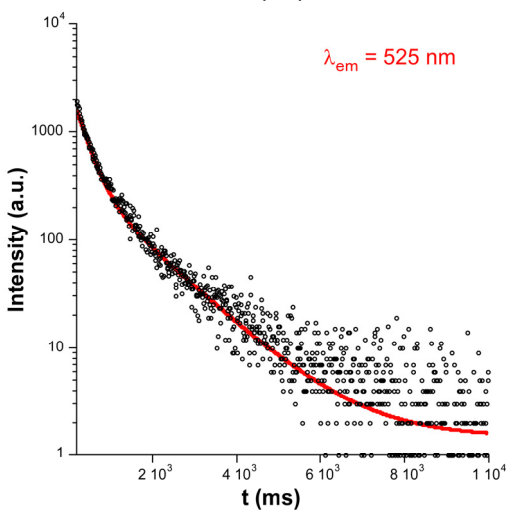
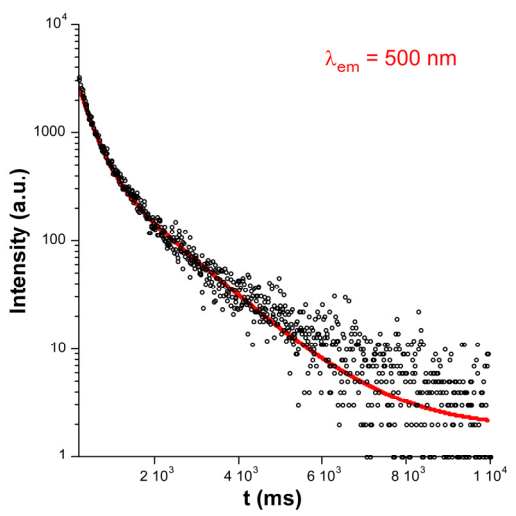
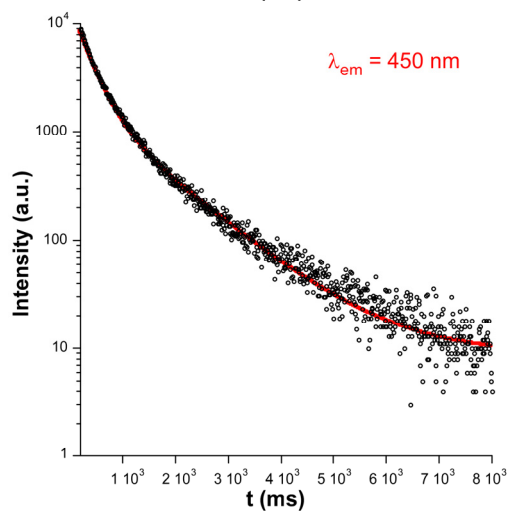
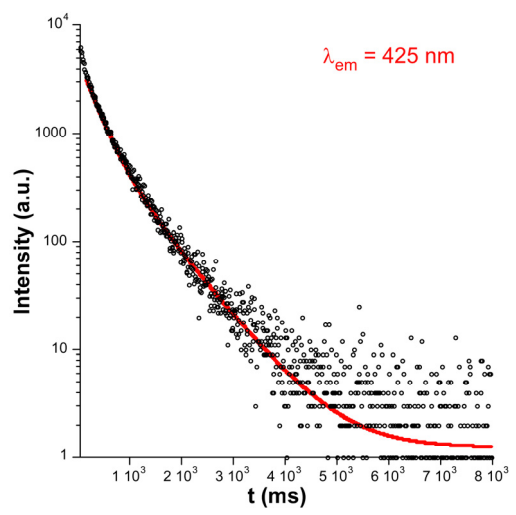
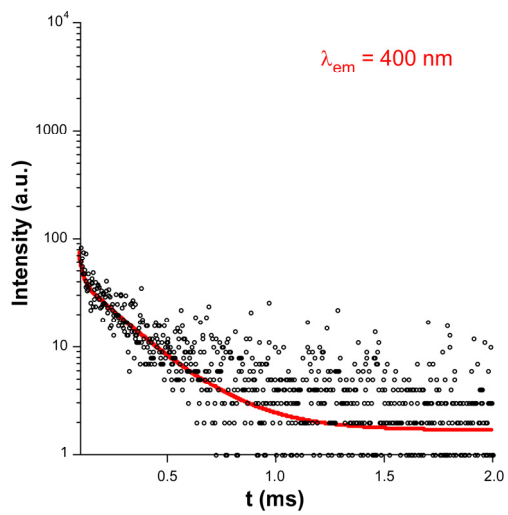


Figure S42. Emission decay curves for compound **4** at selected emission wavelength (every 25 nm in the 400–525 nm range) showing the best fitting.



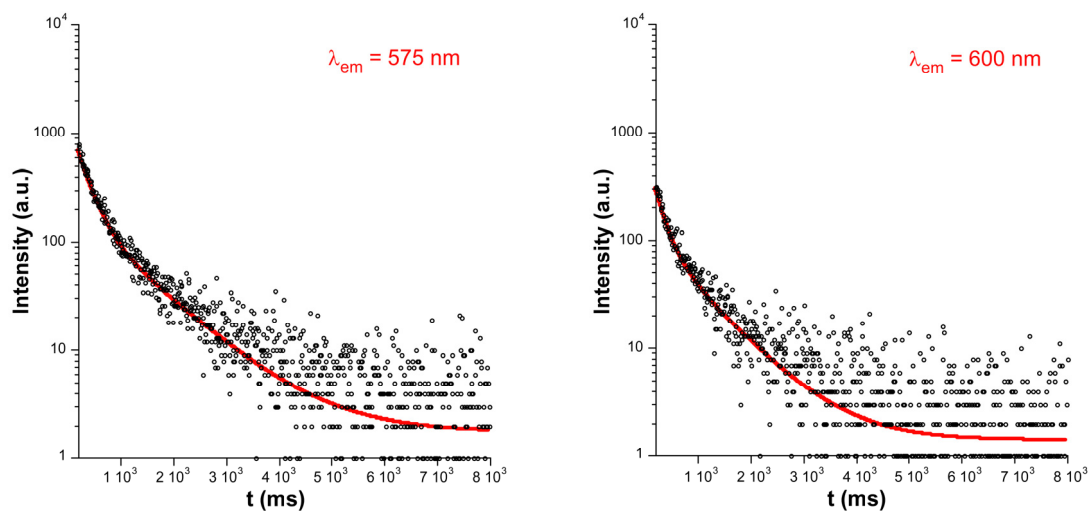


Figure S43. Emission decay curves for compound 5 at selected emission wavelength (every 25 nm in the 400–600 nm range) showing the best fitting.

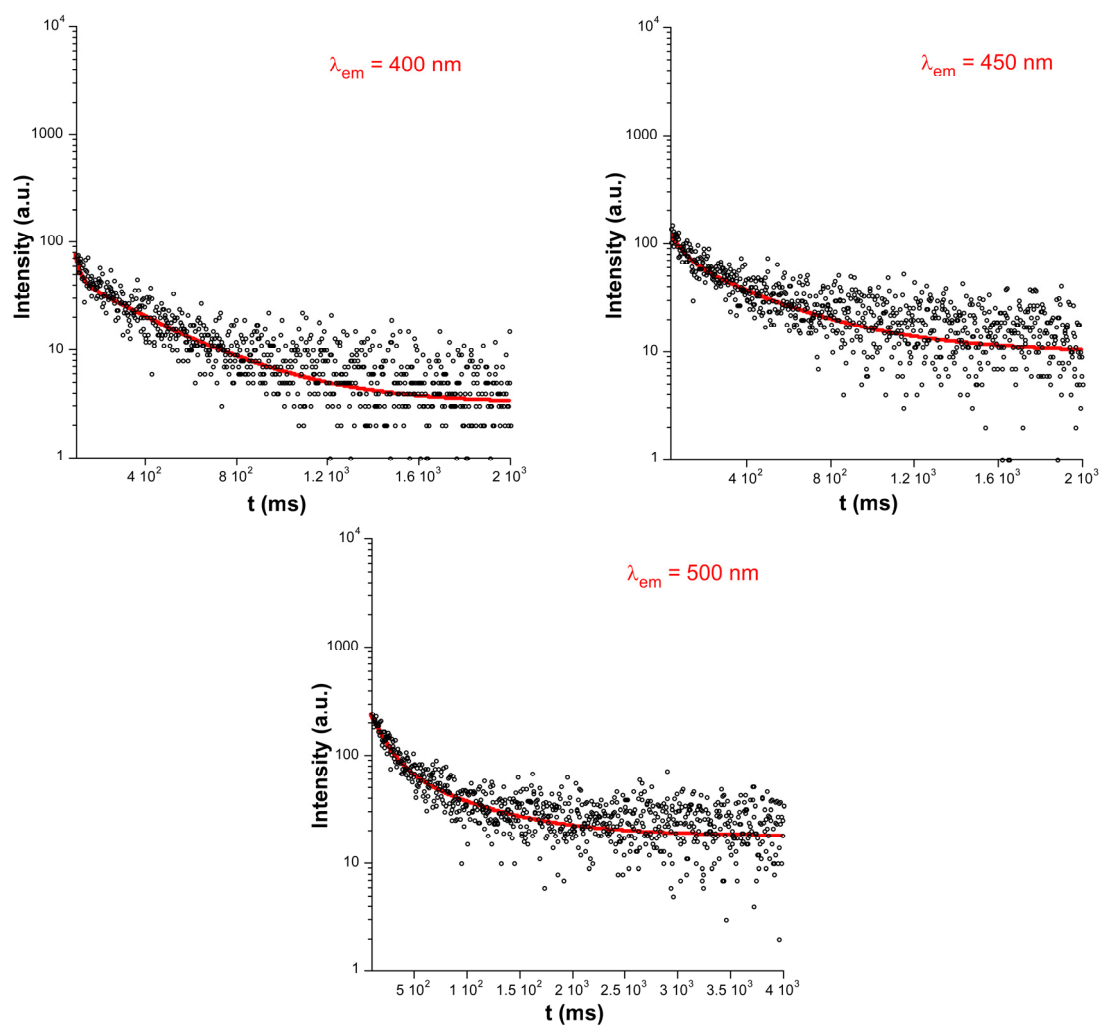


Figure S44. Emission decay curves for compound 6 at selected emission wavelength showing the best fitting.

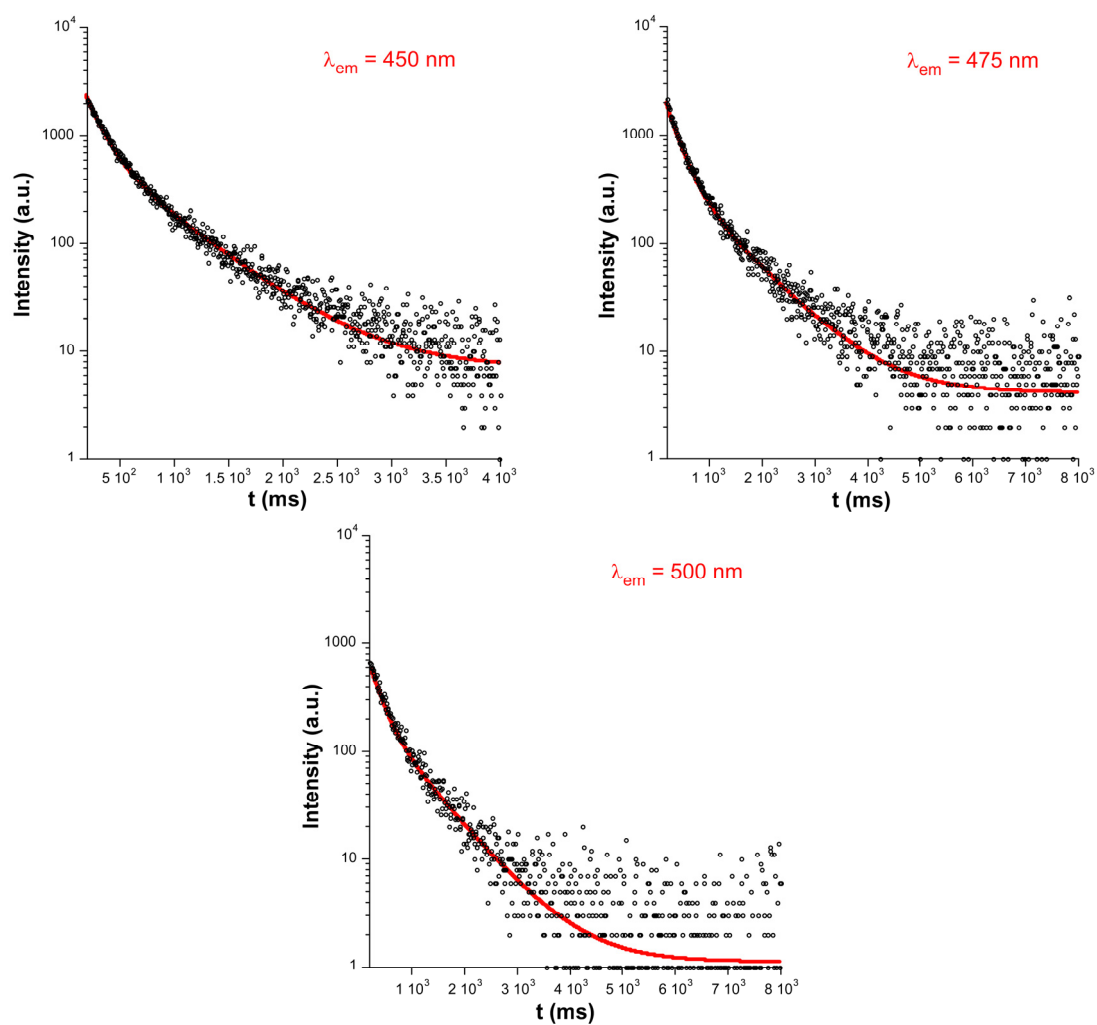


Figure S45. Emission decay curves for compound **4-d** at selected emission wavelengths (around the maximum phosphorescence) showing the best fitting.

Table S14. Values of lifetimes for compounds **4**, **5** and **6** estimated from best fitting of decay curves measured at 10 K accompanied by percentages for the components ($\lambda_{\text{ex}} = 340 \text{ nm}$; $\lambda_{\text{em}} = 400\text{--}600 \text{ nm}$).

Fluorescence emission			
$\lambda(\text{nm})$	$\tau_1 (\mu\text{s})$		Chi Sq.
Compound 4			
400	119(2) / 100%		1.192
Compound 5			
400	115(1) / 100%		1.142
Compound 6			
400	314(1) / 100%		1.135
Phosphorescence emission			
$\lambda(\text{nm})$	$\tau_1 (\text{ms})$	$\tau_2 (\text{ms})$	Chi Sq.
Compound 4			
425	111(4) / 39%	343(10) / 61%	1.138
450	136(3) / 42%	402(10) / 58%	1.158
475	207(2) / 63%	995(9) / 37%	1.172
500	204(2) / 62%	940(12) / 38%	1.131
525	195(4) / 56%	768(15) / 44%	1.385
Compound 4-d			
450	209(2) / 54%	760(6) / 46%	1.152
475	239(2) / 48%	861(6) / 52%	1.137
500	222(5) / 36%	765(9) / 64%	1.163
Compound 5			
425	292(3) / 50%	748(5) / 50%	1.179
450	293(1) / 51%	1108(4) / 49%	1.154
475	317(2) / 49%	1325(6) / 51%	1.190
500	306(2) / 47%	1298(7) / 53%	1.203
525	298(3) / 46%	1237(9) / 54%	1.165
550	272(4) / 43%	1118(11) / 57%	1.173
575	247(3) / 45%	1023(12) / 55%	1.190
600	196(5) / 36%	841(13) / 64%	1.185
Compound 6			
450	66(6) / 10%	421(7) / 90%	1.198
500	149(5) / 32%	705(15) / 68%	1.234

S9. TD-DFT computational details.

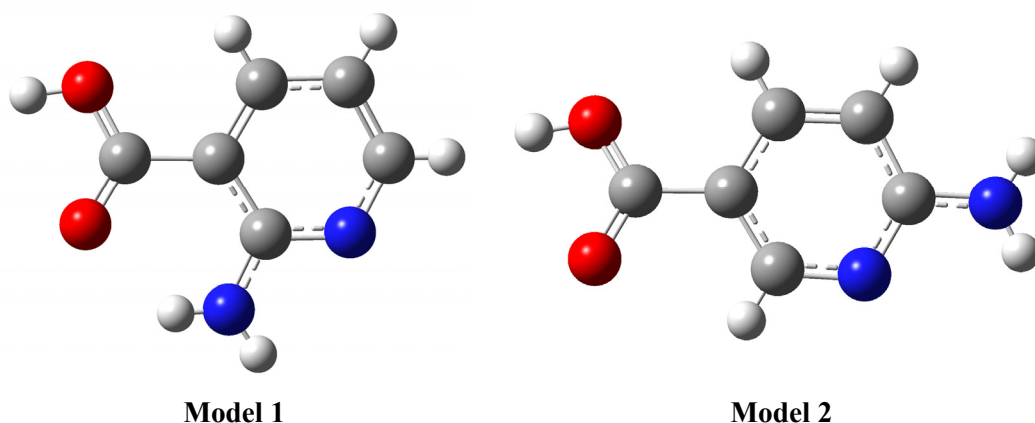


Figure S46. Molecular representation of models of the ligands employed for the calculations.

Table S15. Calculated main excitation and emission energies (nm), singlet electronic transitions and associated oscillator strengths of model **1** in gas phase.

Exp. λ (nm)	Calcd. λ (nm)	Significant contributions	Osc. strength (a.u.)
Excitation energies			
256	270	HOMO \rightarrow LUMO + 1 (69%)	0.0705
267		HOMO - 3 \rightarrow LUMO (13%)	
325	333	HOMO \rightarrow LUMO (96%)	0.120
340			
Emission energies			
385	388	HOMO \leftarrow LUMO (97%)	0.116
393			
465	455	HOMO - 1 \leftarrow LUMO (97%)	0.095

Table S16. Calculated main excitation and emission energies (nm), singlet electronic transitions and associated oscillator strengths of model **2** in gas phase.

Exp. λ (nm)	Calcd. λ (nm)	Significant contributions	Osc. strength (a.u.)
Excitation energies			
255	260	HOMO \rightarrow LUMO (66%) HOMO - 1 \rightarrow LUMO (28%)	0.120
323 337	325	HOMO \rightarrow LUMO (96%)	0.329
Emission energies			
385 395	376	HOMO - 2 \leftarrow LUMO (76%) HOMO \leftarrow LUMO (11%)	0.492
440	437	HOMO \leftarrow LUMO (83%) HOMO - 1 \leftarrow LUMO (14%)	0.095

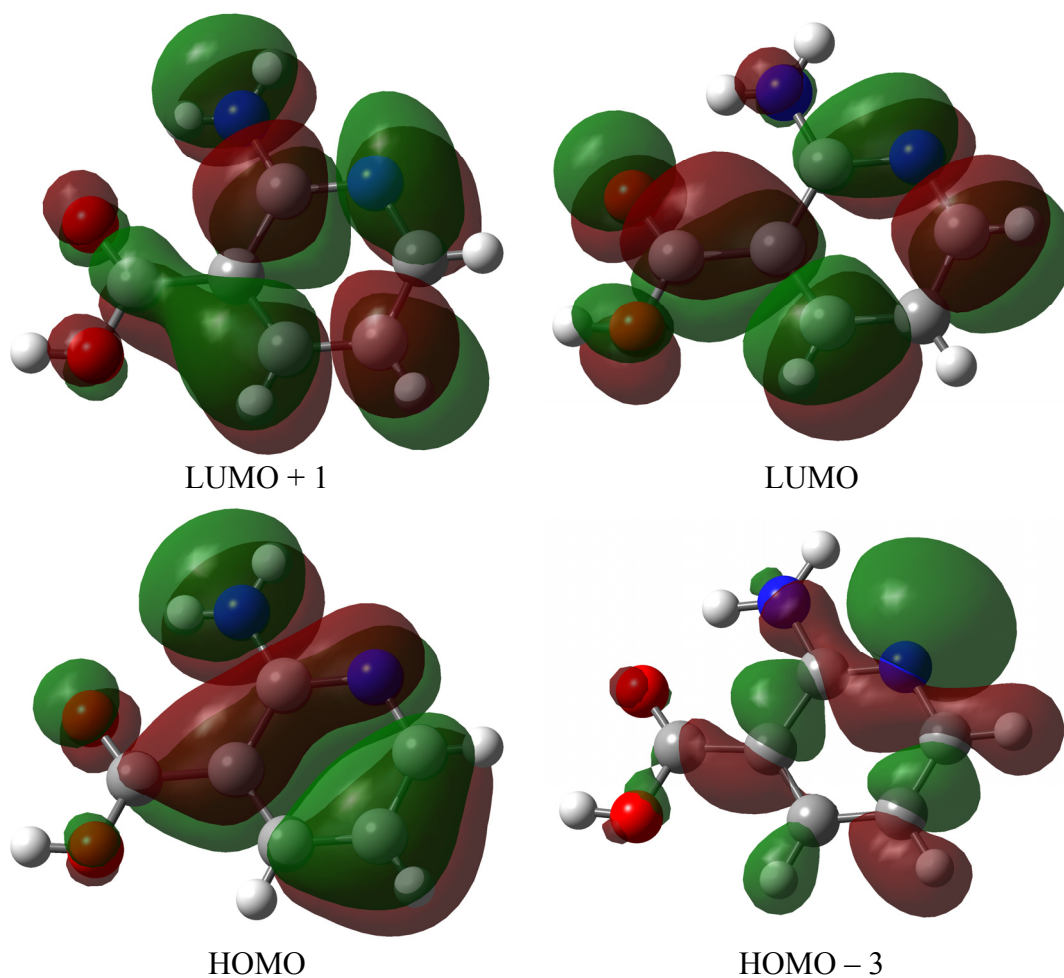


Figure S47. Lowest Unoccupied and Highest Occupied Molecular Orbitals of model **1** involved in the singlet excitation charge transitions.

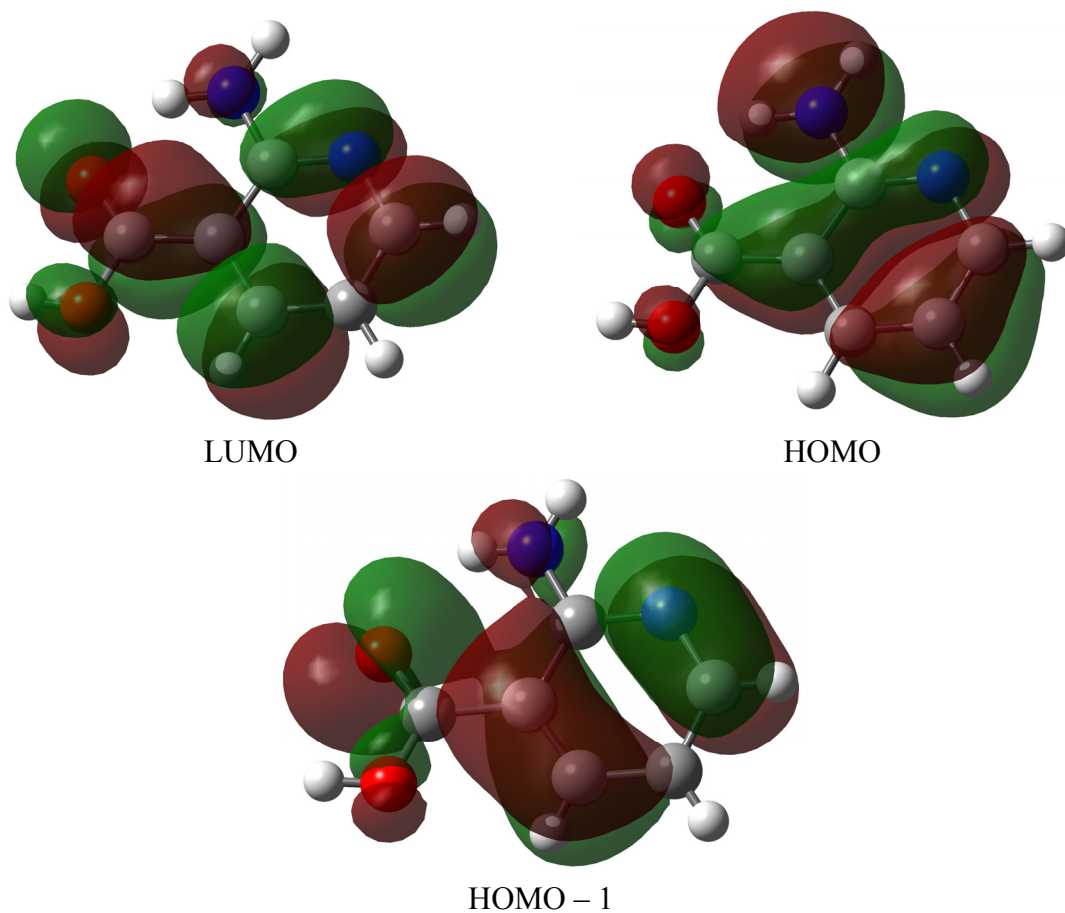


Figure S48. Highest Occupied and Lowest Unoccupied Molecular Orbitals of model **1** involved in the main singlet emission charge transitions.

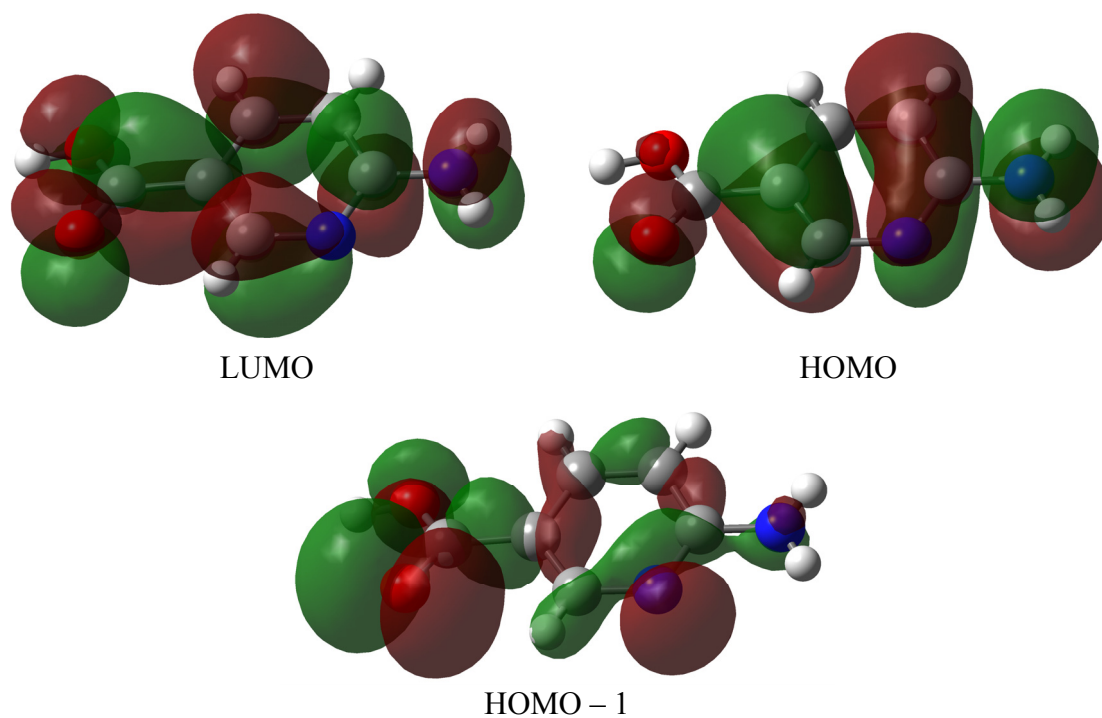


Figure S49. Highest Occupied and Lowest Unoccupied Molecular Orbitals of model **2** involved in the main singlet excitation charge transitions.

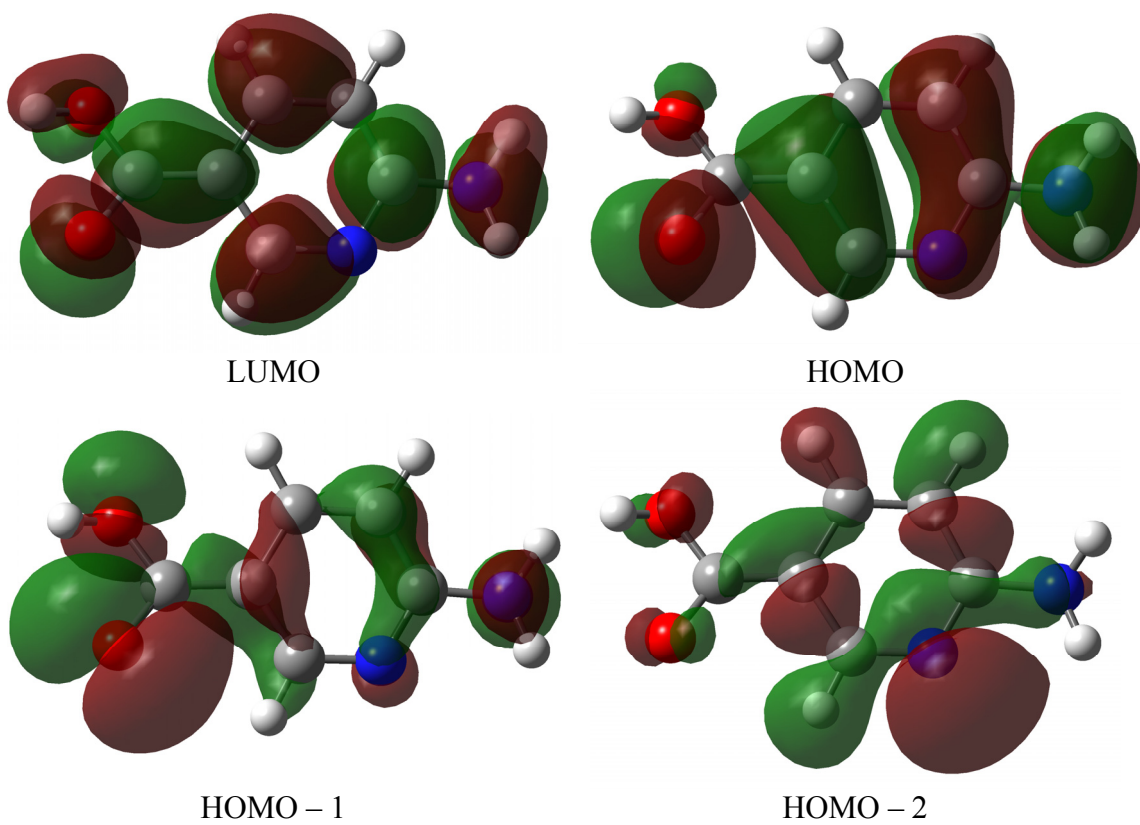


Figure S50. Highest Occupied and Lowest Unoccupied Molecular Orbitals of model **2** involved in the main singlet emission charge transitions.

S10. Calculation of the lowest-lying triplet state (T_1).

The T_1-S_0 energy difference, which corresponds to the main phosphorescent emission line, has been estimated from vertical excitation performed for the optimized geometry of the lowest lying excited triplet state (T_1). The triplet state geometry optimisation and frequencies calculation was performed on models 1 and 2 (Figure S46) with Gaussian 09 package, using the Becke three parameter hybrid functional with the non-local correlation functional of Lee-Yang-Parr (B3LYP) with the 6-311G++(d,p) basis set for all atoms. A fact about these MOs calculated at triplet state geometry that must be emphasized is that they show a similar shape regarding their singlet counterparts, with a π and π^* character respectively for HOMO and LUMO.

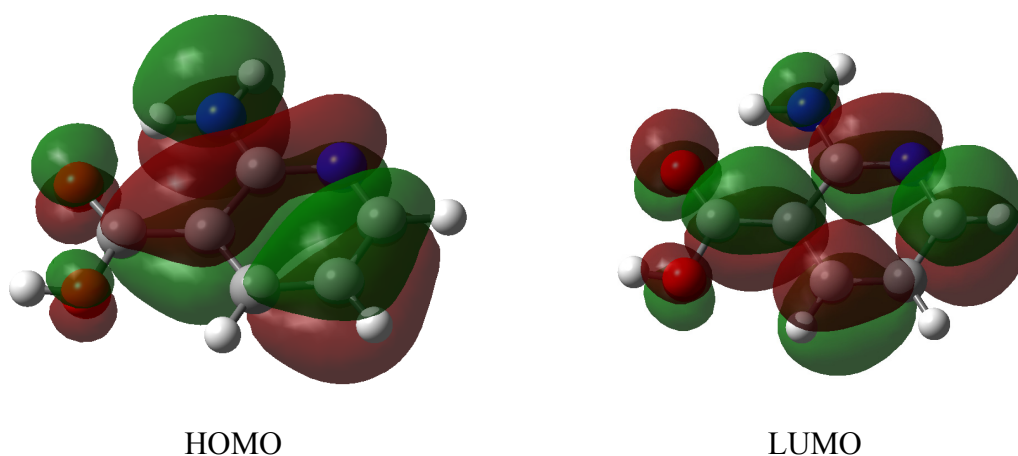


Figure S51. Highest Occupied and Lowest Unoccupied (single-occupied alpha) Molecular Orbitals converged at first excited triplet state geometry for model 1.

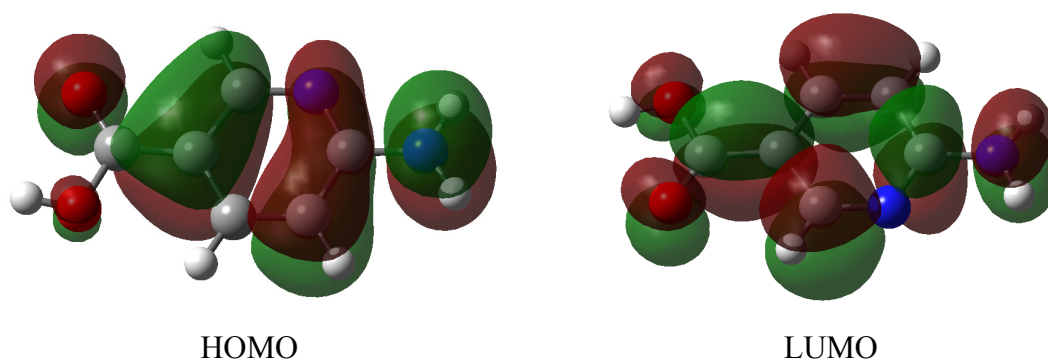


Figure S52. Highest Occupied and Lowest Unoccupied (single-occupied alpha) Molecular Orbitals converged at first excited triplet state geometry for model 2.

S11. PL sensing of compound 4.

The stability of compound **4** in water has been confirmed by collecting the solid remaining filtered from the **4@H₂O** suspension. As observed in Figure S53, the diffractogram of the solid filtered from water suspension corresponds to compound **4**.

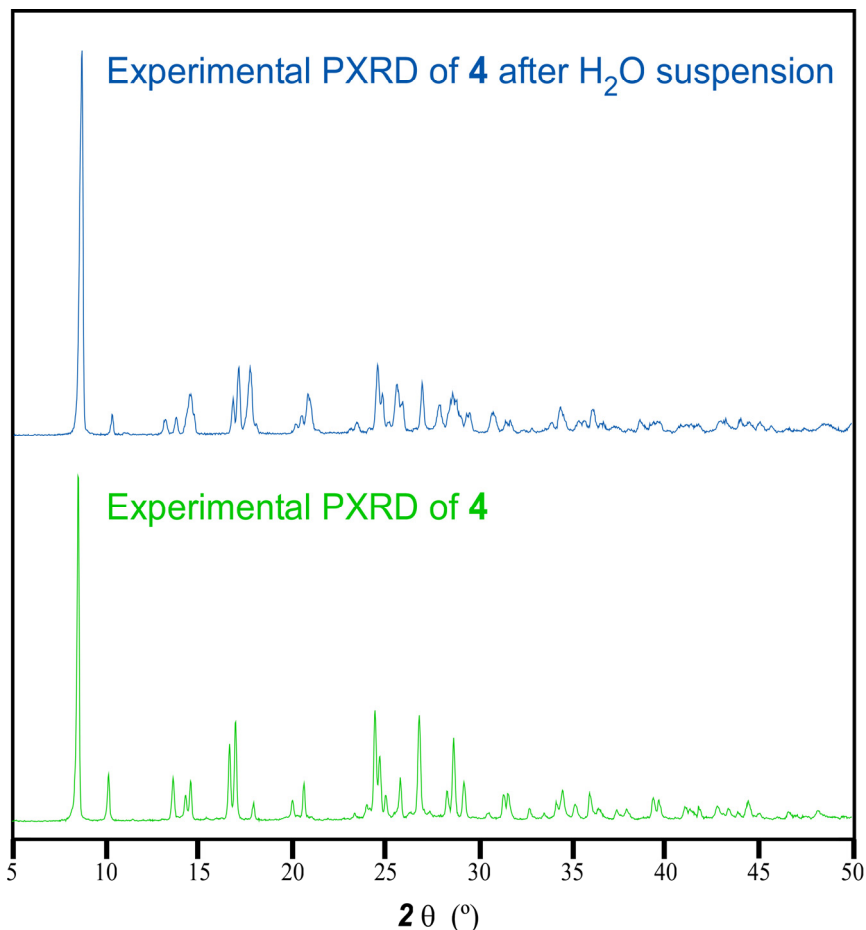


Figure S53. PXR D data for the solid filtered from the **4@H₂O** suspension compared to the diffractogram of pristine compound **4**.

When polycrystalline sample of compound **4** is dispersed in water in order to face sensing activity towards Cu²⁺, it is clearly observed that a copper(II)-based compound precipitates in the solution, indicating that AE ions are exchanged by copper(II) in the compound. PXR D diffractogram measured for that sample corroborates that idea by showing a mixture of phases (initial compound **4** together with an unidentified Cu-6ani compound, see Figure S54).

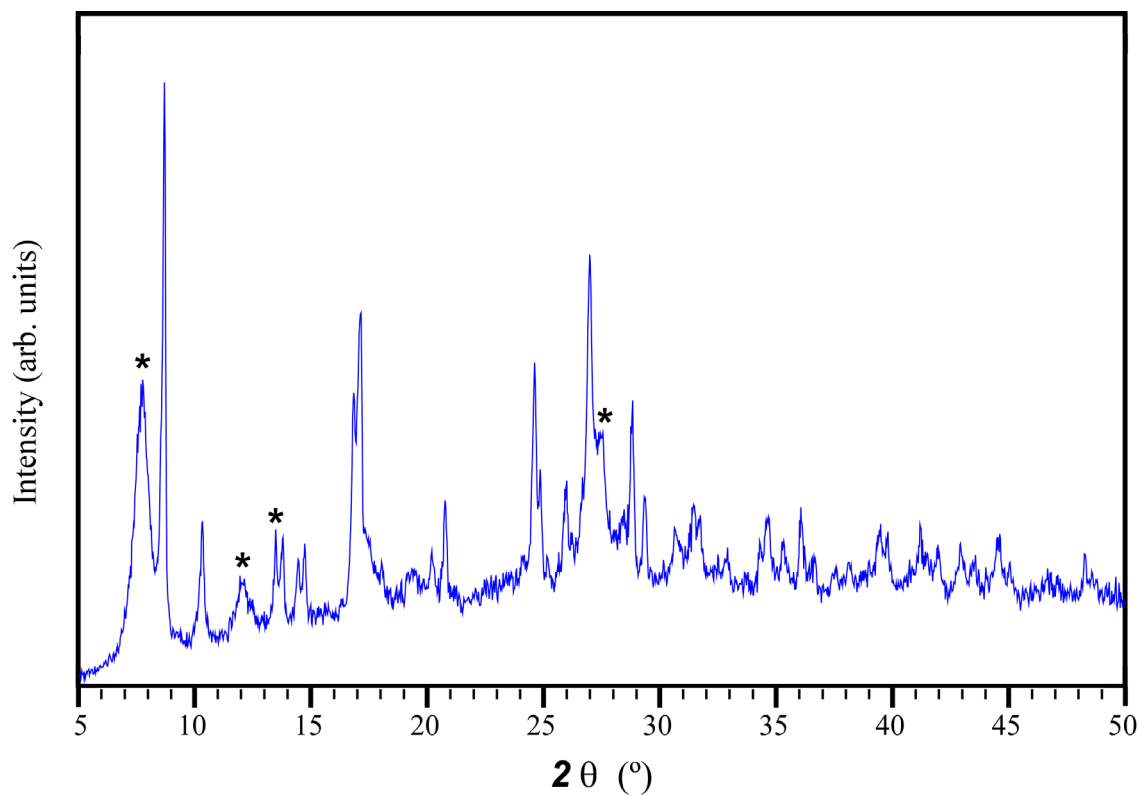


Figure S54. PXRD data for the Cu^{2+} exchanged $4@H_2O$ sample. Diffraction maxima noted with an asterisk represent main diffraction peaks of the copper(II)-6ani compound.

On another level, PL sensing properties of compound **4** in aqueous suspensions have been deeply analyzed for detection of Cr^{3+} and Fe^{3+} given their large quenching compared to other studied ions. The linear dependence of the intensity according to the concentration of Cr^{3+} ions allows data be fitted to the Stern-Volmer equation:

$$I_0/I = 1 + k_{SV}[Q] \quad (\text{eq. 1})$$

On the contrary, Stern-Volmer plot for Fe^{3+} concentration shows a non-linear curve indicating the simultaneous occurrence of dynamic and static quenching. Therefore, the curve has been fitted 2nd order polynomial expression which accounts for both processes:¹

$$I_0/I = (1 + k_{SV}[Q])(1 + k_a[Q]) = 1 + (k_{SV} + k_a)[Q] + k_{SV}k_a[Q]^2$$

where k_{SV} and k_a stand for the constants involving dynamic and static quenching processes. Best fitting results for the polynomial expression give:

$$C = 0.19 \quad (k_{SV} + k_a) = 3935 \quad k_{SV}k_a = 3.66 \times 10^7$$

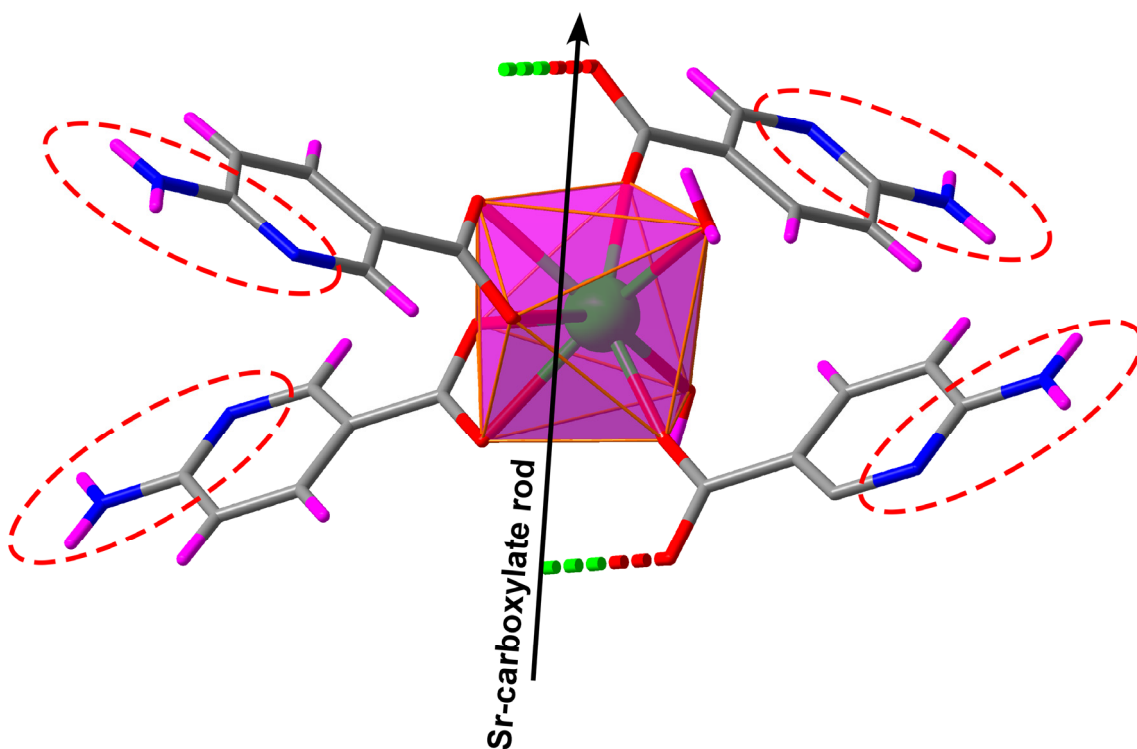


Figure S55. Excerpt of the structure of **4** showing the potential interaction sites (dashed circles).

¹ (a) J. V. Goodpaster and V. L. McGuffin, *Appl. Spectrosc.*, 1999, **53**, 1000–1008. (b) J. Kusba, V. Bogdanov, J. Gryczynski and J. R. Lakowicz, *Biophys J.*, 1994, **5**, 2024–2040.

Stern-Volmer plot was also measured for variable concentration of CrCl₃ salt in order to discard the effect of the counteranions. As observed in Figure S56, an almost undistinguishable curve is obtained, giving a practically identical value of the Stern-Volmer constant.

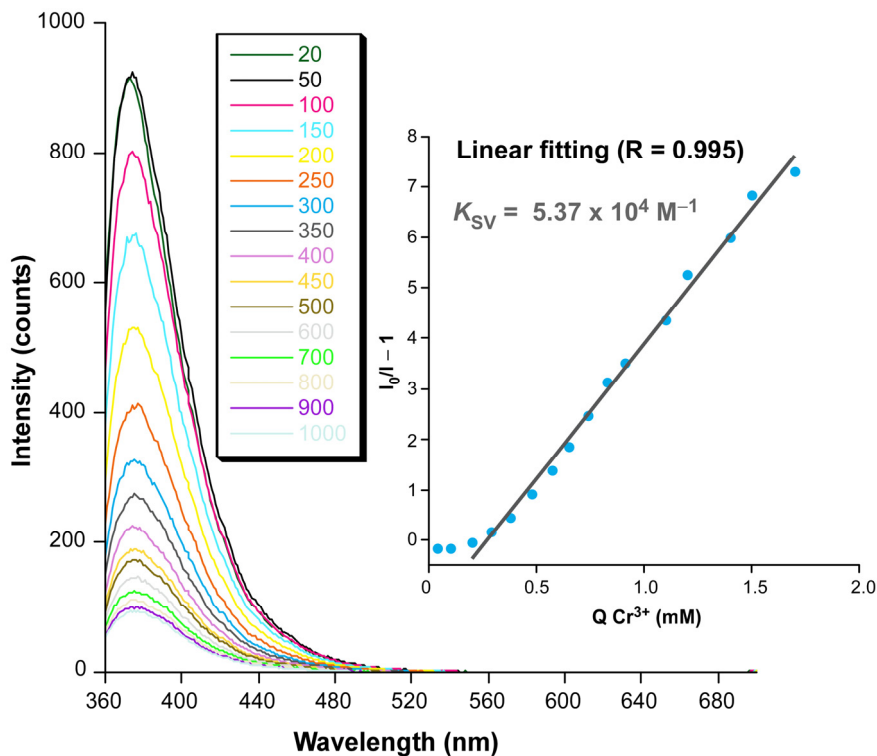


Figure S56. Luminescence quenching of 4@H₂O with gradual addition of CrCl₃ showing the Stern-Volmer plot with the linear fit.

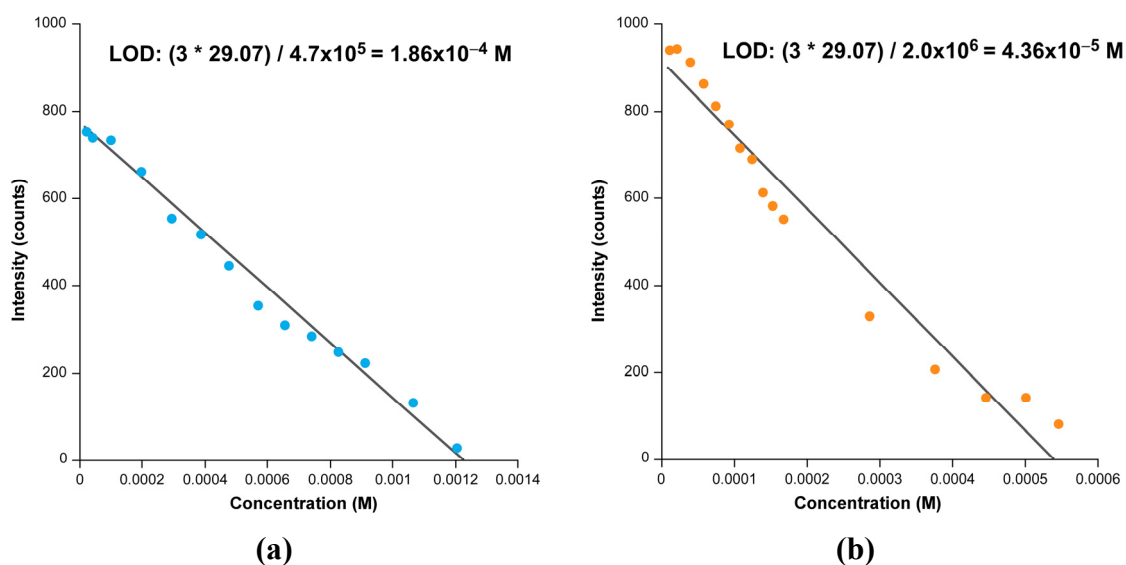


Figure S57. Plots showing the calibration curves to determine the slope for calculating the LOD of compound 4 for (a) Cr³⁺ and (b) Fe³⁺ ions.

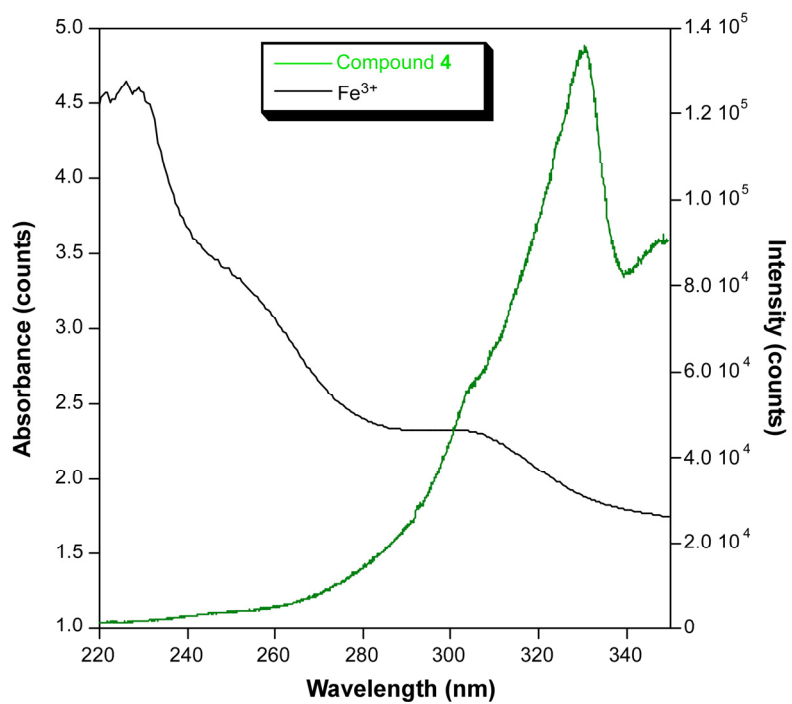


Figure S58. Simultaneous representation of absorbance spectrum of Fe³⁺ solution and excitation spectrum of compound 4.